R. & M. No. 3583

MINISTRY OF TECHNOLOGY

AERONAUTICAL RESEARCH COUNCIL
REPORTS AND MEMORANDA

Calibration of the R.A.E. Bedford 8 ft. × 8 ft. Wind Tunnel at Subsonic Speeds, Including a Discussion of the Corrections Applied to the Measured Pressure Distribution to Allow for the Direct and Blockage Effects Due to the Calibration Probe Shape

By D. Isaacs
Aerodynamics Dept., R.A.E., Bedford

LONDON: HER MAJESTY'S STATIONERY OFFICE
1969
PRICE £1 11*s.* 6*d.* NET

Calibration of the R.A.E. Bedford 8 ft. × 8 ft. Wind Tunnel at Subsonic Speeds, Including a Discussion of the Corrections Applied to the Measured Pressure Distribution to Allow for the Direct and Blockage Effects Due to the Calibration Probe Shape

By D. ISAACS
Aerodynamics Dept., R.A.E., Bedford

Reports and Memoranda No. 3583*
February, 1968

Summary.

A calibration of the 8 ft × 8 ft wind tunnel has been performed at subsonic speeds using a multiple orifice, traversing, static pressure probe on the tunnel centreline.

Full details have been obtained of the static pressure distribution along the tunnel centreline between 69 inches upstream and 50 inches downstream of the tunnel datum. Additional measurements were made of tunnel wall static pressure distributions.

Modifications to the nozzle profile, introduced just prior to the present calibration in order to reduce the size of the static pressure gradient, proved successful.

LIST OF CONTENTS

*Replaces R.A.E. Technical Report 67038 – (A.R.C. 29 310).

---

1. *Introduction.*

An important design feature of the 8 ft × 8 ft wind tunnel is that it can be used not only as a supersonic tunnel but also as a subsonic variable pressure tunnel. As such, it is an important facility because of the ease with which Mach number and Reynolds number can be independently varied.

A high proportion of the testing at subsonic speeds is in connection with accurate drag measurements of models of transport aircraft at high subsonic speeds. This type of investigation poses quite severe demands on the uniformity of flow throughout the working section, and an accurate flow calibration becomes an absolute necessity. In particular, accurate drag measurements require that any pressure gradients present along the tunnel centreline are known to high accuracy. For example, it is well known[1] that for any body of volume V the buoyancy drag coefficient, ΔC_D, due to a linear pressure gradient of dp/dx, is given by,

$$\Delta C_D = \frac{V}{q\,S}\,\frac{dp}{dx},$$

where q is the freestream kinetic pressure and S the reference area. Typically, for models of transport aircraft, $V = 1500$ to 4500 cu inches and $S = 550$ sq inches, so that in order to know ΔC_D to an accuracy of 0·0001, it is necessary to know $\frac{1}{q}\frac{dp}{dx}$ to an accuracy of 0·000012 to 0·000036 per inch.

Previous calibration of the 8 ft × 8 ft had shown the existence of significant pressure gradients along the tunnel centreline, although the calibration technique then used did not enable these to be measured to the required accuracy. Consequently, in addition to performing an accurate flow calibration, it was decided to attempt to eliminate or reduce this gradient over the Mach number and Reynolds number ranges where accurate drag measurements were most required, *viz.* $M = 0{\cdot}60$ to 0·90, and $R/l = 6 \times 10^6$ per ft. A preliminary calibration was made at $M = 0{\cdot}74$, $R/l = 6 \times 10^6$ per ft to measure accurately the pressure gradient, the appropriate profile modifications were calculated and introduced into the shape of the nozzle, and a comprehensive calibration was then undertaken.

This calibration of the tunnel was performed during March 1965.

2. *Description of the Wind Tunnel.*

The 8 ft × 8 ft wind tunnel is a continuous flow, closed circuit, tunnel with a working section 8 ft square. The Mach number range covered by the tunnel is from zero to 2·8, but excludes the transonic regime. The maximum total pressure at which the tunnel can operate varies between 115 inches mercury absolute and 25 inches mercury absolute, dependent on Mach number, and the minimum is 3 inches mercury absolute at all Mach numbers. The stagnation temperature can be controlled to some extent, roughly ±10 deg C about a mean value, but the level of the mean value depends to a large extent on the power being developed by the compressor and on the external ambient temperature. The level of water vapour in the tunnel can be controlled by means of air drying equipment such that the frost point can be maintained at less than −30 deg C at all Mach numbers.

The tunnel is powered by means of an axial flow compressor driven by one synchronous a.c. motor of 68 000 h.p. and two d.c. motors each of 6000 h.p., giving a total available power of 80 000 h.p. or 60 MW. There is facility for changing the number of stages in the compressor between 4 and 10, the former being used at subsonic speeds and for supersonic Mach numbers up to $M = 2{\cdot}0$, and the latter principally for supersonic Mach numbers between 2·0 and 2·8. Where testing on a model requires a Mach number range extending from subsonic speeds up to $M = 2{\cdot}8$, it is possible to use the 10 stage compressor over the whole of this range, but a penalty is incurred in respect of maximum allowable total pressure at Mach numbers below 2·0. For further details of the compressor Reference 2 should be consulted.

The settling chamber is of octagonal cross section and has an area of some 997 sq ft, giving a contraction ratio into the working section of 15.6:1. Although there is provision in the settling chamber for mounting 2 gauze screens, none, are at present fitted.

The roof and floor of the nozzle and working section (Fig. 1) consist of two flexible steel plates, 62 ft long, mounted between two rigid parallel side walls. The nozzle profile, appropriate to the required working section Mach number, is obtained by deforming the two steel plates by means of a system of screw jacks driven by hydraulic motors, and controlled by a hydraulic servo system with the aid of auxiliary screws, from data supplied electrically from punched tapes. A full description of the construction and operation of the nozzle is given by Barnes and Dunham[3], and of the method used in setting the nozzle by Winter[4].

For sting mounted models, the model attitude in pitch is remotely controlled by means of a quadrant driven by a hydraulic motor, and rotating about a virtual centre on the tunnel centreline, 4 ft upstream of the flexible plate hinge (on the schlieren window centreline). This location is referred to throughout the Report as the tunnel datum. The model can also be remotely rolled about the sting centreline.

A fixed fairing behind the quadrant extends downstream for approximately 36 ft or almost the length of the supersonic diffuser (Fig. 2). This is where the supersonic flow from the working section (when the tunnel is operating at supersonic speeds) is decelerated to subsonic speeds by means of a system of oblique shock waves generated both by the quadrant leading edge and an adjustable ramp formed by the leading section of the supersonic diffuser wall. The entire supersonic diffuser consists of 4 steel plates of total

length 55 ft connected together by hinged or sliding joints and actuated by 3 hydraulic screw jacks. Using these screw jacks, both the tunnel second throat area and the leading-edge ramp angle are adjusted automatically to give optimum pressure recovery characteristics at all supersonic Mach numbers. In addition a 4th screw jack is arranged to operate an air ejector door at Mach numbers above 2·0. This is used primarily to increase the tunnel mass flow at Mach numbers where the mass flow through the nozzle is low and so improve the match with the compressor characteristics. The air flow through the ejectors is extracted from the settling chamber through slots around the periphery and is by-passed around the working section to the ejector nozzles, the pressure differential existing between the settling chamber and the supersonic diffuser being sufficient to ensure an adequate supply of air. The use of the supersonic diffuser during subsonic running is described below in Section 3. Aft of the supersonic diffuser is the subsonic diffuser leading to the compressor.

3. *Operation of the Wind Tunnel.*

It is convenient, first, to give a brief description of the power supply to the compressor motors. The supply to the two d.c. motors is obtained from a Ward-Leonard set, which consists of two similar d.c. machines used as generators driven by a synchronous a.c. motor of 14 000 h.p. which is reactor started. The power supply to this a.c. motor is obtained from the Central Electricity Authority 50 c/s grid. The 68 000 h.p. synchronous a.c. motor can be operated either from the 50 c/s grid supply at a fixed synchronous speed of 750 rpm, or alternatively from a variable frequency a.c. supply obtained from a local gas turbine powered generating station. The latter consists of two gas turbine powered generator units, each developing 20 MW at 50 c/s and capable of operation down to 10 c/s where each unit develops $8\frac{1}{2}$ MW. Full details of this variable frequency power installation are given by McKearney *et al*[5].

The adopted procedure for starting the wind tunnel, governed principally by the limited power of the d.c. motors, is to evacuate the tunnel circuit down to a total pressure of 3 inches mercury absolute when the tunnel is to be run up to supersonic speeds. For subsonic operation it is not necessary to reduce the tunnel total pressure to as low a value as 3 inches mercury absolute (Fig. 3). The two d.c. motors, driving the a.c. motor and the compressor, are then run up to the synchronous speeds of the a.c. motor, and on synchronization, the tunnel total pressure is increased to the required value.

It is possible to operate the tunnel in two distinct ways at subsonic speeds. One method uses the variable frequency a.c. supply, and obtains the required Mach number in the working section by varying the compressor speed. The supersonic diffuser profile is identical for all Mach numbers (Fig. 2), and the jack settings used correspond to those given in Table 1 for $M = 0{\cdot}98$. The alternative method is to run the compressor at a more or less constant speed, and choke the tunnel flow in the supersonic diffuser by forming a throat between the trailing edge of the leading panel and the quadrant (Fig. 2). The range of throat areas so obtained enables the working section Mach number to be varied between a lower limit of 0·60 and an upper limit of 0·98 in intervals of 0·01. Because of the dependence of the working section Mach number on choked conditions at the throat, the static-pressure distribution along the two leading panels of the supersonic diffuser has to be monitored throughout the tests, to ensure the existence of a region of supersonic flow terminated by a shock wave aft of the throat. This is of most importance when operating at the upper limit of available power, where reduction in compressor speed can be used to achieve slightly higher values of tunnel total pressure.

Because of the lower efficiency of the supersonic diffuser when running with the tunnel choked (loss of total pressure through shock waves) there is a reduction in available total pressure compared with unchoked running conditions (Fig. 3). However, there is one great advantage in that the working section flow is steadier and free from low frequency oscillations which are present with the tunnel unchoked. An additional benefit which is demonstrated in Section 10.1 is the increased length of working section which is free from the upstream influence of the supersonic diffuser and quadrant pressure fields.

The performance curves for operation at subsonic speeds with the 4-stage compressor and variable frequency a.c. supply are shown in Fig. 3. Shown in Fig. 4 is the variation in compressor speed with Mach number for the 4-stage compressor with the tunnel both choked and unchoked, and for the 10-stage compressor with the tunnel unchoked. The rpm against M curves associated with unchoked conditions give a mean value of rpm measured over the entire range of total pressure. A detailed analysis demonstrates

that rpm varies with total pressure and the appropriate values for the 4 stage compressor at different total pressures are given in Table 2.

It is possible to run at subsonic speeds with the tunnel choked and the compressor speed constant at 750 rpm (power from 50 c/s grid supply). There is, however, an additional loss in efficiency due to the increased extent of supersonic flow in the supersonic diffuser and consequently stronger shock waves, which result from the increased pressure ratio available at the higher rpm. This results in a further reduction in available total pressure at any Mach number.

The use of the 10-stage compressor at subsonic speeds, as previously mentioned, also incurs a penalty in respect of maximum allowable total pressure.

4. *Scope of Present Calibration.*

It is important that the results of the tunnel calibration should be compatible with the existing test-data reduction computer program, so that it is appropriate here to give some details of the latter.

At supersonic speeds, the kinetic pressure (q), which is used to reduce measured forces and pressures, etc., to non-dimensional coefficient form, is derived from measured values of the tunnel total pressure (H_0) and Mach number. Tabulated values of the ratio H_0/q are readily obtainable, and convenient to use, so that the principal parameter required from a calibration at supersonic speeds is the variation of Mach number along the length of the working section at different values of tunnel total pressure.

At subsonic speeds, H_0/q varies more rapidly with Mach number especially at the lower Mach numbers, and so is very inconvenient to use since a small error in Mach number can introduce quite large errors in kinetic pressure. The use of the parameter $H_0 - p_0/q$, where p_0 is the working section static pressure, overcomes this difficulty, since it displays only a small variation with Mach number up to $M = 1{\cdot}0$. Since the difference between total and static pressures, $H_0 - p_0$, is usually recorded during tunnel tests, it involves no further pressure measurements than those normally made. Values of H_0/q and $H_0 - p_0/q$ are compared in the following Table.

M	H_0/q	$H_0 - p_0/q$
0	∞	1·0000
0·1	143·86	1·0025
0·2	36·724	1·0100
0·3	16·896	1·0227
0·4	9·969	1·0406
0·5	6·778	1·0641
0·6	5·062	1·0933
0·7	4·044	1·1286
0·8	3·403	1·1704
0·9	2·983	1·2192
1·0	2·704	1·2756

The 8 ft × 8 ft tunnel computing program for data reduction is based on the use of $H_0 - p_0$ and H_0 as the starting point in the derivation of kinetic pressure q and Mach number M at subsonic speeds, and in addition it attempts to correct $H_0 - p_0$, q and M for blockage effects using the measured changes in wall pressure opposite the model. This technique for obtaining blockage corrections has been described by several authors, e.g. Thom and Jones[6], Mair and Gamble[7] and Evans[8]. Quite simply, it involves using linear theory to calculate the ratio of the blockage velocity increment on the tunnel centreline at the position of the model to the total velocity increment (direct + blockage) at the tunnel wall. This factor is then used to obtain the centreline blockage increment from the measured change in wall pressures due to the model. A simplified model configuration is usually assumed in the calculations, e.g. a body represented by a source-sink combination with the wings replaced by a line doublet or a line source and line

sink combination etc. The blockage velocity at the model can be calculated either as a mean value over the model length or alternatively the velocity at a particular point on the model can be used, i.e. it can be chosen to suit a particular type of investigation. The main advantage of this technique over the use of calculated values of the blockage velocity increment at the model, is that the uncertainty in the allowance for Mach-number effects in the theory is reduced, i.e. it is assumed that the Mach-number effect on the centreline blockage velocity increment and on the wall total velocity increment are identical.

At subsonic speeds the reference static pressure is obtained from the side wall static-pressure hole No. 32, which is situated far enough upstream to be free from model blockage effects (*see* Table 3). This is measured on a 0 to 30 inches of mercury range capsule-type manometer[9] as H_0-p_{32}. The derivation of H_0-p_0 is as follows,

$$(H_0-p_0)_i = (H_0-p_{32})_i - \left[\frac{\Delta p_0}{H_0-p_{32}}\right](H_0-p_{32})_i + \frac{\lambda}{4}\sum_{j=1}^{4}(H_0-p_{wj})_i - \lambda\,(H_0-p_{32})_i\,, \tag{1}$$

where the suffix i refers to a particular 'wind-on' measurement. The term in the square brackets,

$$\left[\frac{\Delta p_0}{H_0-p_{32}}\right], = \left[\frac{p_c-p_{32}}{H_0-p_{32}}\right] - \frac{\lambda}{4}\sum_{j=1}^{4}\left[\frac{p_{wj}-p_{32}}{H_0-p_{32}}\right], \tag{2}$$

where p_c = empty tunnel centreline static pressure at the position of the model, and

p_{wj} = empty tunnel wall static pressure at the position of the model.

(Since the exact position of the peak suction on the tunnel wall may not be known before the test starts, it is often convenient to measure the pressure at 4 wall holes at the position of the model (j = 1 to 4), 2 on the upper wall and 2 on the lower wall. The computation is arranged to take a mean value of these 4 measurements as shown above.)

λ = ratio of the mean blockage correction to the tunnel centreline pressure to the peak pressure decrement at the tunnel walls. Typical values of $1/\lambda$ are given by Thom and Jones[6] for both bodies of revolution and wings. The computer evaluates H_0-p_0/H_0 and uses fitted polynomials to evaluate H_0-p_0/q and M. In the above expression for H_0-p_0, it is assumed that during the tunnel test, the wall pressures $(H_0-p_{wj})_i$ have been measured on capsule manometers having a resolution of 0·01 inch mercury and a range of 30 inches mercury. It is possible to measure these wall pressures as $(p_{wj}-p_{32})_i$ on capsule manometers having a range of 6 inches mercury and a resolution of 0·001 inch mercury. In this case the expression for $(H_0-p_0)_i$ becomes,

$$(H_0-p_0)_i = (H_0-p_{32})_i - \left[\frac{\Delta p_0}{H_0-p_{32}}\right](H_0-p_{32})_i - \frac{\lambda}{4}\sum_{j=1}^{4}(p_{wj}-p_{32})_i\,. \tag{3}$$

The present tunnel calibration, then, must yield values of $\frac{p_c-p_{32}}{H_0-p_{32}}$ and $\frac{p_w-p_{32}}{H_0-p_{32}}$ over the whole range of Mach numbers and Reynolds numbers at which the tunnel can operate, and in addition, the magnitude and extent of any pressure gradient along the working section centreline must be accurately determined.

5. *Details of Probe and Wall Pressure Holes.*

The probe consists of a circular cross section cylindrical steel tube 2·25 inches in diameter and 50 inches long (Fig. 5). It has a semi-ellipsoidal nose 6·75 inches long, and behind the parallel portion, a straight taper flare over a distance of 12 inches to a diameter of 2·50 inches.

The probe has a total of 25 static pressure orifices, 0·030 inch in diameter, at intervals of 2·00 inches along 1 generator, with the leading pressure hole situated 1 inch behind the probe shoulder (forward end of parallel portion). Each pressure hole is contained by a steel plug of maximum diameter 0·44 inch and having a taper of 0·05 inch per inch on diameter. These plugs were made overlong and were forced into a series of tapered holes spaced along the probe, and locked in position using a proprietary liquid locking agent. The nose section was added and the probe was then ground to a smooth finish. Finally, any burrs present in the pressure holes were carefully removed, taking care not to chamfer the hole in the process. Despite this elaborate manufacturing technique, with great care taken to get as near perfect a hole as possible, the static pressure coefficient as measured by adjacent holes differed by up to $\pm 0{\cdot}001$ (Fig. 6). This sort of difficulty in obtaining accurate static pressure measurements has been experienced by other workers[10] in this field.

It was originally intended to use the probe as a fixed probe mounted on the tunnel centreline with the probe datum on the quadrant centre of rotation. However, there were some reservations about the accuracy with which pressure gradients could be measured using a fixed probe, and the streamwise extent of the measurements was rather limited. Consequently, it was decided to mount the probe on the tunnel calibration gear sting. This supports the calibration probes used in calibration of the tunnel at supersonic speeds, and has been used to a limited extent during early subsonic calibrations. The calibration-gear sting consists of a circular cross-section steel tube of 4·5 inches diameter, and capable of translation along the tunnel centreline over a total distance of 90 inches (Fig. 5). The fore and aft motion of the sting is obtained using a screw jack system driven by a hydraulic motor. The present probe was mounted on a tapered adaptor, 5·49 inches long, at the front of the sting. At the junction of the moving sting and the quadrant, there are two fixed hemisphere-cylinder fairing caps situated one behind the other. The difference between these fairing caps and the single cap normally used during sting-mounted model tests is clearly shown in Fig. 7.

A boundary-layer transition strip was applied to the nose of the probe. This consisted of ballotini of diameter 0·0041 inch to 0·0049 inch glued to the nose by a thin layer of adhesive in a 0·25 inch wide band located 1·50 inches from the apex. This strip was calculated to be sufficient to promote boundary-layer transition close behind the strip for Reynolds numbers of 3×10^6 per ft and above.

Static-pressure orifices are located along the entire length of the tunnel from the settling chamber to the subsonic diffuser. From the settling chamber to 3 ft 6 inches upstream of the schlieren window centreline there are a series of holes along the centreline of the port wall of the tunnel. Additionally the first seven stations in the settling chamber also have holes in the top and bottom walls. In the working section there are a series of holes on the centreline of the top and bottom walls, extending from 61 inches upstream of the schlieren window centreline to 36 inches downstream of that point. In the supersonic diffuser 31 pressure holes are situated along the port wall centreline and 10 along the starboard wall centreline. The windswept surfaces of the tunnel from the settling chamber to the supersonic diffuser are coated with a thin layer of Araldite (about 0·007 inch thick) worked to a smooth finish. It is not easy to drill perfectly circular holes through this coating, and several of the pressure holes have ragged edges with chips of Araldite missing etc. In order that the pressure distribution along the tunnel, as measured by the wall holes, should not be affected by further deterioration of the pressure holes, steel inserts were fitted to 10 of the top and bottom wall holes in the working section, and to the subsonic reference static hole before the present calibration. Full details of the static pressure hole distribution are given in Table 3.

6. *Details and Accuracy of Pressure Measurements.*

22 probe pressures were measured on a single pressure transducer of range ± 5 lb per sq inch using a 24 to 1 way pressure switch. The subsonic reference static pressure (tunnel side wall hole No. 32) was used as the transducer reference pressure. The transducer measurements were displayed on a strip chart recorder and recorded using the 8 ft $\times$ 8 ft tunnel transducer-system punched-card output. The calibration factor of the transducer on the range used for the tests, and hence the theoretical resolution of the measurements, was 0·001 inch mercury per count.

With the exception of number 73 bottom-wall circuit which was leaking badly and impossible to cure, all the working section top and bottom wall pressures were measured on an inclined (30° to horizontal)

multi-tube water manometer. The tunnel reference static was also measured on the manometer, the reference pressure for which was side wall hole No. 31. The water manometer was situated inside the tunnel pressure shell on the same level as the working section. The manometer readings were monitored by closed circuit T.V. and recorded photographically. The calibration factor of the water manometer was 0·0362 inch mercury per inch water. The resolution of the water manometer scale can be taken as roughly $\frac{1}{40}$ inch which yields a theoretical pressure measurement resolution of approximately 0·001 inch mercury.

It is estimated that the accuracy of the measured values of the pressure coefficient $\frac{p-p_{32}}{H_0-p_{32}}$ are as follows:

(a) pressure-coefficient difference as measured by the same probe pressure hole

± 0·00015	tunnel choked
± 0·00075	tunnel unchoked

(b) overall level of pressure coefficient as measured by any probe pressure hole

± 0·001	tunnel choked
± 0·005	tunnel unchoked

(c) overall level of pressure coefficient as derived by the method of Section 9.1

± 0·0003	tunnel choked
± 0·0015	tunnel unchoked

(d) pressure coefficient as measured by any wall hole

± 0·0002	tunnel choked
± 0·0010	tunnel unchoked

(e) pressure coefficient gradient, $\frac{1}{H_0-p_{32}}\frac{dp}{dx}$ per inch

± 0·000004	tunnel choked
± 0·000020	tunnel unchoked

The above figures refer to the accuracy of individual readings, the accuracy of the final mean faired curves should be somewhat better.

7. *Calibration Procedure.*

As described in the Introduction the first part of the present calibration involved an attempt to eliminate as far as possible the pressure gradient along the working section centreline with the tunnel choked for $M = 0{\cdot}60$ to 0·90 and $R/l = 6 \times 10^6$ per ft. With the original nozzle profile (*see* Table 4), and at a Mach number of 0·74, the probe was advanced along the tunnel centreline, as described below, and the static pressure distribution as measured by probe hole number 14 was used to determine the gradient. This was compared with the assumed pressure gradient which had been used to calculate a new nozzle profile, and the change in ordinates was adjusted to suit the measured gradient. The nozzle shape was then modified (Fig. 8 and Table 4) and the calibration repeated when the gradient was found to be much smaller (Fig. 9). This modified tunnel centreline pressure distribution was deemed adequate, and the modified nozzle profile was adopted. That the modification was successful in minimising the pressure gradient over the range $M = 0{\cdot}60$ to 0·90, $R/l = 6 \times 10^6$ per ft, is clearly shown by Figs. 9 and 21.

For the detailed calibration of the working section with the nozzle profile modified as above, the procedure adopted at each condition (Mach number, Reynolds number combination, Fig. 3), was to start with the probe in its aft position with the probe datum 39 inches behind the centre of rotation of the quadrant, the probe was then advanced, usually in intervals of 2·5 inches, to a position with the probe datum 46 inches forward of the quadrant centre of rotation. In general, at each location, only three probe pressures were recorded, numbers 2, 14 and 23, but with the probe at 4 locations (probe datum 19 inches

aft, 1 inch, 21 inches and 41 inches forward of the quadrant centre of rotation) all 22 probe pressures were recorded together with the upper and lower wall pressures. For some unchoked conditions the intervals in probe movement were increased to 5 inches and all 22 probe pressures were recorded at each location.

8. *Corrections to Measured Pressures.*

For static pressure probes which have pressure holes at one location only, it is possible at subsonic speeds, to design the probe such that the pressure fields from the probe nose and probe support effectively cancel each other. In the present case where the static pressure distribution along the probe is measured by 22 holes, such an interference-free design is of course impossible. An attempt was made, therefore, to calculate the static-pressure error at each hole due to the probe nose, sting flare, etc., and to apply appropriate corrections to the measured pressures.

Using linear theory, the tunnel centreline pressure distributions, both direct and blockage, were calculated for the probe nose (Figs. 10 and 11), the probe sting flare (Figs. 12 and 13) and the difference in sting fairing caps as used with the calibration sting and a typical model sting (Fig. 14). Full details of the calculations are given in Appendices A and B. Similar calculations were performed for the tunnel-wall pressure distributions due to the various probe components. In the case of the difference in sting fairing caps, the pressure field along the wall was negligibly small. Since the wall pressures were recorded with the probe at 4 different locations along the tunnel centreline, it was possible to analyze the wall pressures and to derive directly from them the pressure distribution (direct + blockage) on the tunnel walls due to the probe nose and the probe sting flare. The method of analysis is given in Appendix C. A comparison between measured pressure distributions due to the probe nose and sting flare and distributions calculated using linear theory is shown in Fig. 15 for Mach numbers of 0·30, 0·65, 0·82 and 0·90. The agreement between measured and calculated distributions is quite good, which suggests that linear-theory calculations of corrections to the centreline pressures will also probably be of adequate accuracy.

The static-pressure error due to hole size was calculated for the probe pressure holes from the results of experiments by Shaw[10]. It was assumed that the probe boundary layer was turbulent from the leading edge and that Shaw's results were independent of Mach number. Values of the calculated static-pressure error are given in Fig. 16 and details of the internal shape of the probe static pressure holes in Fig. 17.

9. *Analysis of Pressure Measurements.*

9.1. *Centreline Pressures.*

As described in the calibration procedure a complete data readout of all 22 probe pressures was made at 4 probe locations only (with the probe datum located at -19 inches, $+1$ inch, $+21$ inches and $+41$ inches measured forward from the tunnel datum). Between the limits of probe travel (probe datum 39 inches aft of tunnel datum to 46 inches forward of tunnel datum), three probe pressures were recorded at intervals of 2·5 inches or 5·0 inches.

For the partial data readout, probe pressure numbers 2, 14 and 23 were corrected for the difference in sting fairing caps, and were then plotted against the distance from the tunnel datum, x. From this plot the extent and magnitude of the linear gradient were accurately determined. As an example, Fig. 18 shows the pressure distribution along the centreline as measured by probe holes 2, 14 and 23 at $M = 0{\cdot}74$, $R/l = 6 \times 10^6$ per ft with the tunnel choked. The mean pressure gradient measured here, $\frac{1}{H_0 - p_{32}} \frac{dp}{dx}$, is 0·0000075, and the extent of the linear gradient is from -69 inches to $+12$ inches measured downstream of the tunnel datum (the limit of the linear gradient is defined as the value of x at which the actual variation of $\frac{p - p_{32}}{H_0 - p_{32}}$ with x has deviated from the linear variation by 0·0005).

For each of the 4 complete data readouts (all probe pressures measured), all the pressures were corrected both for the difference in sting fairing caps and for the probe nose, probe sting flare, and hole-size errors. The analysis of the method of 'least squares' yields 2 simultaneous equations,

$$\left.\begin{aligned} \sum_{1=1}^{n} x_i P_i - a\sum_{i=1}^{n} x_i^2 - b\sum x_i &= 0 \\ \sum_{i=1}^{n} P_i \quad - a\sum_{i=1}^{n} x_i - nb \qquad &= 0 \end{aligned}\right\} \left(P_i = \frac{p_i - p_{32}}{H_0 - p_{32}}\right) \tag{4}$$

the solution of which enables the slope, a, and the intercept, b, of a set of n experimental points to be determined. Since the slope, a, has already been determined the intercept, b, is readily obtained as,

$$b = \frac{\sum_{i=1}^{n} P_i - a\sum_{i=1}^{n} x_i}{n} \tag{5}$$

The intercept was obtained by applying this equation to all points obtained in the 4 complete data readouts, within the following limitations,

(a) Values of x were used only where there were at least 2 values of $\frac{p-p_{32}}{H_0-p_{32}}$ (obtained from 2 of the 4 complete readouts, i.e. $-44 < x < +18$). This restriction was applied on the assumption that any errors in p due to pressure holes with slightly rounded or chamfered edges would be reduced in size and might possibly cancel each other, by taking a mean of 2 or more pressures (Rayle[11] has shown that both positive and negative errors in the measured pressure can be introduced by variations in the orifice edge form).

(b) Values of x were used, only where the gradient was linear. Having determined both the slope and the intercept of the static pressure distribution curve, the values of $\frac{p-p_{32}}{H_0-p_{32}}$ obtained during the partial data readout were adjusted so that they all coincided at identical values of x, and passed through the intercept point at $x = 0$ (or the extrapolation of the linear part of the curve passed through the intercept point at $x = 0$). Fig. 19 illustrates the method of obtaining the intercept from the 4 complete data readouts and Fig. 20 shows the final static-pressure distribution along the tunnel centreline, obtained at $M = 0{\cdot}74$, $R/l = 6 \times 10^6$ per ft with the tunnel choked.

9.2. *Wall Pressures.*

The only analysis here involved correcting the measured wall pressures for the direct and blockage effects of the probe nose and probe sting flare using the measured corrections derived in Section 8 (Fig. 15). Since the wall holes are used during model tests to measure a change in pressure only (due to model blockage) it was not necessary to correct the pressure for hole size effects.

10. *Discussion of Results.*

The tunnel centreline and tunnel-wall static-pressure measurements, following the analysis detailed in Section 9, are shown in Figs. 24 to 34 and 35 to 46 respectively. These results apply to the empty tunnel with a single sting fairing cap in position near the leading edge of the quadrant (Fig. 7(b)), but with no sting present. For tunnel tests where the model is sting supported, the results must be corrected for the direct and blockage effects of the sting and for the blockage effects of the model.

It should be noted that, in all tables and figures, unless stated otherwise, the Mach number quoted for the data is derived from the reference static hole (side wall hole No. 32) for the tunnel unchoked data, and

is the nominal Mach number for the tunnel choked data. Table 5 summarizes, for the tunnel choked condition, the differences between the nominal Mach number, the Mach number derived from wall hole No. 32, and the Mach number at the tunnel datum.

10.1. *Centreline Pressures.*

The magnitude and extent of the linear pressure gradient on the tunnel centreline and the intercept of the linear pressure gradient with the tunnel datum ($x = 0$) are shown in Figs. 21, 22 and 23 respectively. In general, Mach number and Reynolds number have a large effect on both the magnitude of the pressure gradient and on the intercept with the tunnel datum, although the extent of the linear pressure gradient is independent of Reynolds number and is affected by Mach number only to a small extent. It should be noted that the effect of choking the tunnel at $M = 0{\cdot}60$ and $0{\cdot}65$ is to alter slightly the magnitude of the pressure gradient and the intercept with the tunnel datum. There is a more marked difference between the values of the extent of the linear pressure gradient with the tunnel choked and unchoked. As was stated in Section 7, the attempt, by means of nozzle profile modifications, to minimise the pressure gradient over the Mach number range 0·60 to 0·90 with the tunnel choked and $R/l = 6 \times 10^6$, was clearly successful (Fig. 21).

Figs. 24 to 34 which show the variation of the pressure coefficient, $\frac{p-p_{32}}{H_0-p_{32}}$, with distance along the tunnel centreline for various Mach number, Reynolds number combinations, require little comment. Worth noting, is the extremely good collapse of the data from the different probe pressure holes at all conditions with the tunnel choked. The scatter which exists in the data for the tunnel unchoked, is principally due to the unsteadiness in the tunnel flow which was mentioned previously in Section 3.

The abrupt rise in pressure, which characterizes the upstream influence of the quadrant and supersonic diffuser pressure fields, clearly limits the length of models which can be tested at subsonic speeds. This is especially true where accurate drag measurements are required, and where the model afterbody is of such a shape that the flow around it is at all sensitive to interference effects, e.g. models of subsonic transport aircraft having rear mounted engine nacelles.

10.2. *Wall Pressures.*

Figs. 35 to 46 show the variation with Mach number and Reynolds number of the pressure coefficient $\frac{p-p_{32}}{H_0-p_{32}}$ for each working section upper and lower wall hole. As in the case of the tunnel centreline pressure distribution, these are virtually self explanatory. The wall pressure, as measured by the most upstream of the holes, shows very little difference between the tunnel choked and unchoked conditions at $M = 0{\cdot}60$ and $0{\cdot}65$, whereas holes downstream of the tunnel datum show a large difference which becomes even more pronounced the further the hole is from the tunnel datum. This effect is a further demonstration of the upstream influence of the quadrant and supersonic diffuser pressure fields.

A slightly unusual feature is that although for the majority of the holes a progressive variation of pressure coefficient with Mach number and Reynolds number is obtained, in a few cases, e.g. 57 top and 70 top, the variation with Reynolds number is inconsistent and irregular. It should be noted that neither of these two pressure holes was modified by the fitting of a steel insert before the present calibration (c.f. Section 5), and inspection of the holes revealed that the Araldite coating was chipped and irregular around the edge of the pressure hole. It is suggested that the inconsistent variation of the pressure coefficient is due entirely to the irregular shape of the pressure hole, i.e. the variation with Reynolds number of the pressure coefficient increment due to the irregular shape is of the opposite sense to the variation with Reynolds number of the basic pressure coefficient as measured by a perfectly circular hole.

For completeness, Fig. 47 shows the variation of static pressure with Mach number as measured by various tunnel side-wall holes. This data was not obtained during the present calibration but has been obtained during routine tunnel tests. It is included, since it is often necessary to obtain a pressure intermediate between working section static and total pressure for use as a reference or calibration pressure

during pressure measurement tests using the 8 ft × 8 ft transducer readout system. The measured values are compared with theory based on one-dimensional isentropic flow and ignoring boundary-layer growth on the nozzle walls.

11. *Conclusions.*

A calibration of the 8 ft × 8 ft wind tunnel has been performed at subsonic speeds. Using a multiple orifice, traversing, static-pressure probe, the following details of the flow in the working section have been accurately determined for various combinations of Mach number and Reynolds number,

(1) The magnitude and extent of the linear pressure gradient on the tunnel centreline.

(2) The intercept of the linear pressure gradient with the tunnel datum (centre of rotation of quadrant).

(3) The static pressure distribution along the tunnel centreline between 69 inches upstream and 50 inches downstream of the tunnel datum.

In addition, the working section top- and bottom-wall pressure distributions and the nozzle side-wall pressure distributions have been measured.

A modification to the nozzle profile, which was introduced just prior to the present calibration in order to reduce the size of the tunnel centreline static-pressure gradient, was proved successful.

Acknowledgement.

The author wishes to acknowledge the work of J. Hall who was responsible for the design of the modified nozzle shape.

LIST OF SYMBOLS

a	Slope of a set of experimental points
b	Intercept of a set of experimental points } *see* equation (4)
C_D	Drag coefficient $= \dfrac{\text{drag force}}{qS}$
C_p	Pressure coefficient $= \dfrac{p-p_0}{q}$
C_{p_1}	Tunnel centreline blockage pressure coefficient due to an isolated source on the centreline of a tunnel of square cross section
C_{p_2}	Tunnel wall centreline total pressure coefficient (direct + blockage) due to an isolated source on the centreline of a tunnel of square cross section
C_p^*	Asymptotic value of stream pressure coefficient a large distance downstream from the nose of a semi-infinite body (equivalent to a source at $x = 0$ and sink at $x = \infty$) $C_p^* = -2S/\beta^2 h^2$
h	Tunnel height
H_0	Tunnel total pressure
m	Source strength
M	Mach number
M_{32}	Mach number at side-wall pressure hole No. 32
M_{C_L}	Mach number on the tunnel centreline at the quadrant centre of rotation
M	Integers denoting location of image sources used in the calculation of blockage pressure
N	fields
p	Static pressure
p_0	Free stream or working section static pressure
p_{32}	Static pressure at side-wall pressure hole No. 32
Δp_0	*See* equation (2)
p_w	Empty tunnel, wall static pressure at the position of the model
p_c	Empty tunnel, centreline static pressure at the position of the model
P	Pressure coefficient $= \dfrac{p-p_{32}}{H_0-p_{32}}$
q	Kinetic pressure
r	Radial distance measured from x-axis in polar co ordinate system
R	Radius of body of revolution
R/l	Reynolds number per foot
S	Model reference area
S	Cross-sectional area of body of revolution
U	Free stream or empty tunnel velocity
u	Perturbation velocity parallel to 0x

REFERENCES

No.	*Author(s)*	*Title, etc.*
1	H. Glauert	Wind tunnel interference on wings, bodies and airscrews. A.R.C. R. & M. 1566 (1933).
2	L. J. Cheshire, ... J. Y. G. Evans, W. A. Goodsell and P. H. W. Wolff	The design and construction of the compressor for the 8 ft × 8 ft High Speed Wind Tunnel at R.A.E. Bedford. *Proc. Inst. Mech. Eng.* Vol. 172, No. 15 (1958).
3	T. Barnes and .. .. .. C. R. Dunham	Automatic setting of the flexible walls of a large wind tunnel. *Proc. Inst. Elec. Eng. 105*, Part A, No. 21 (1958).
4	K. G. Winter	Methods used in setting the 8 ft × 8 ft wind tunnel variable supersonic nozzle. R.A.E. Technical Note Aero 2912 (1963) (A.R.C. 25694).
5	P. McKearney and .. .. L. S. Drake and E. G. Mallalieu	A variable frequency power installation for large wind tunnel drives. *Proc. Inst. Elec. Eng. 105*, Part A, No. 21 (1958).
6	A. Thom and .. .. .. M. Jones	Tunnel blockage near the choking condition. A.R.C. R. & M. No. 2385 (1946).
7	W. A. Mair and .. .. H. E. Gamble	The effect of model size on measurements in the R.A.E. high speed tunnel. Drag of two-dimensional symmetrical aerofoils at zero incidence. A.R.C. R. & M. No. 2527 (1944).
8	J. Y. G. Evans	Corrections to velocity for wall constraint in any 10 ft × 7 ft rectangular subsonic wind tunnel. A.R.C. R. & M. No. 2662 (1949).
9	G. F. Midwood and .. .. R. W. Hayward	An automatic self-balancing capsule manometer. A.R.C. C.P. 231 (1955).
10	R. Shaw	The influence of hole dimensions on static pressure measurements. *Jour. of Fluid Mechanics*, Vol. 7, Part 4, pp. 550–564 (1960).
11	R. E. Rayle	Influence of orifice geometry on static pressure measurements. U.S.A. ASME paper 59–A–234 (1959).
12	—	High Speed Aerodynamics and Jet Propulsion, Vol. VI. *General Theory of High Speed Aerodynamics*, Oxford University Press (1955).

u_1	Blockage perturbation velocity on the tunnel centreline due to an isolated source on the centreline of a square-section tunnel
u_2	Total perturbation velocity (direct + blockage) on the tunnel wall centreline due to an isolated source on the centreline of a square section tunnel
u^*	Asymptotic value of stream total perturbation velocity a large distance downstream from the nose of a semi-infinite body (equivalent to a source at $x = 0$ and sink at $x = \infty$) $u^* = US/\beta h^2$
V	Volume of model fuselage
x, y, z	Cartesian co ordinate system with origin on centreline of square cross section tunnel, x increasing downstream
Y, Z	Particular values of y and z used in the calculation of blockage pressure fields
β	$(1-M^2)^{\frac{1}{2}}$
λ	Ratio of mean blockage correction to the tunnel centreline pressure to the peak pressure decrement at the tunnel walls
Π_1	u_1/u^* or C_{p_1}/C_p^*
Π_2	u_2/u^* or C_{p_2}/C_p^*
φ	Perturbation velocity potential
θ	Semi included angle of probe sting flare
ξ	Alternative dimension to x (*see* Fig. 48)

APPENDIX A

Calculation of Direct Pressure Field of Various Probe Components.

With the assumptions of subsonic linear theory[1,2] the perturbation velocity potential at a point (x, r) due to a slender axi-symmetric body is given by,

$$\varphi_{(x,r)} = -\frac{U}{4\pi}\int_{\xi_0}^{\xi_1} \frac{S'(\xi)\,d\xi}{[(x-\xi)^2+\beta^2 r^2]^{\frac{1}{2}}}, \tag{A.1}$$

where U is the free stream velocity, $S(\xi)$ is the local cross sectional area of the body (the prime denotes differentiation with respect to ξ, distance measured along the body axis), x and r are polar co ordinates of the point at which φ is being evaluated (Fig. 48), and $\beta = \sqrt{1-M^2}$, where M is the free stream Mach number.

A.1. *Probe nose*

The equation of the generator of the nose is,

$$\left(\frac{r}{R}\right)^2+\left(\frac{\xi}{\xi_0}\right)^2 = 1$$

and

$$S = \pi r^2 = \pi R^2\left[1-\left(\frac{\xi}{\xi_0}\right)^2\right] \quad \text{(Fig. 48)}$$

therefore

$$S'(\xi) = -\frac{2\pi R^2 \xi}{\xi_0^2}.$$

Substituting for $S'(\xi)$ in the expression for φ gives

$$\varphi = \frac{UR^2}{2\xi_0^2}\int_{\xi_0}^{0} \frac{\xi\,d\xi}{[(x-\xi)^2+\beta^2 r^2]^{\frac{1}{2}}}$$

and

$$\frac{\partial\varphi}{\partial x} = -\frac{UR^2}{2\xi_0^2}\int_{\xi_0}^{0} \xi\frac{\partial}{\partial\xi}\left[\frac{1}{[(x-\xi)^2+\beta^2 r^2]^{\frac{1}{2}}}\right]d\xi$$

$$= -\frac{UR^2}{2\xi_0^2}\left\{\left[\frac{\xi}{[(x-\xi)^2+\beta^2 r^2]^{\frac{1}{2}}}\right]_{\xi_0}^{0} - \int_{\xi_0}^{0}\frac{d\xi}{[(x-\xi)^2+\beta^2 r^2]^{\frac{1}{2}}}\right\}$$

$$= -\frac{UR^2}{2\xi_0^2}\left\{\left[\frac{\xi}{[(x-\xi)^2+\beta^2 r^2]^{\frac{1}{2}}}\right]_{\xi_0}^{0} + \left[\sin h^{-1}\left(\frac{x-\xi}{\beta r}\right)\right]_{\xi_0}^{0}\right\}.$$

Now

$$C_p = -\frac{2}{U}\frac{\partial \varphi}{\partial x} - \frac{1}{U^2}\left(\frac{\partial \varphi}{\partial r}\right)^2 \quad \text{(Ref. 12)} \tag{A.2}$$

$$C_p = -\frac{2}{U}\frac{\partial \varphi}{\partial x} - \left(\frac{\partial r}{\partial x}\right)^2.$$

But since we wish to evaluate C_p only on the parallel portion of the probe or on the tunnel wall, we have,

$$\frac{dr}{dx} = 0$$

therefore

$$C_p = -\frac{2}{U}\frac{\partial \varphi}{\partial x}. \tag{A.3}$$

Substituting for $\partial\varphi/\partial x$ in the expression for C_p, (equation (A.3)), and expanding yields,

$$C_p = -\left(\frac{R}{\xi_0}\right)^2 \left\{ \frac{\xi_0}{[(x-\xi_0)^2+\beta^2 r^2]^{\frac{1}{2}}} - \sin h^{-1}\left(\frac{x}{\beta r}\right) + \sin h^{-1}\left(\frac{x-\xi_0}{\beta r}\right) \right\}. \tag{A.4}$$

A.2. *Probe sting flare*

Here $S = \pi[R+(\xi-\xi_0)\tan\theta]^2$ (*see* Fig. 48)

therefore

$$S'(\xi) = 2\pi \tan\theta\,[R+(\xi-\xi_0)\tan\theta]$$

and

$$\varphi = -\frac{U\tan\theta}{2}\int_{\xi_0}^{\xi_1} \frac{R+(\xi-\xi_0)\tan\theta}{[(x-\xi)^2+\beta^2 r^2]^{\frac{1}{2}}}\,d\xi$$

$$= -\frac{U\tan\theta}{2}\left\{ (R-\xi_0\tan\theta)\int_{\xi_0}^{\xi_1} \frac{d\xi}{[(x-\xi)^2+\beta^2 r^2]^{\frac{1}{2}}} + \int_{\xi_0}^{\xi_1} \frac{\xi\tan\theta}{[(x-\xi)^2+\beta^2 r^2]^{\frac{1}{2}}}\,d\xi \right\}$$

Now

$$\frac{\partial\varphi}{\partial x} = \frac{U\tan\theta}{2}\left\{ (R-\xi_0\tan\theta)\int_{\xi_0}^{\xi_1} \frac{\partial}{\partial\xi}\left(\frac{1}{[(x-\xi)^2+\beta^2 r^2]^{\frac{1}{2}}}\right)d\xi + \tan\theta\int_{\xi_0}^{\xi_1} \xi\frac{\partial}{\partial\xi}\left(\frac{1}{[(x-\xi)^2+\beta^2 r^2]^{\frac{1}{2}}}\right)d\xi \right\}$$

$$= \frac{U\tan\theta}{2}\left\{ \left[\frac{R-\xi_0\tan\theta+\xi\tan\theta}{[(x-\xi)^2+\beta^2 r^2]^{\frac{1}{2}}}\right]_{\xi_0}^{\xi_1} - \tan\theta\int_{\xi_0}^{\xi_1} \frac{d\xi}{[(x-\xi)^2+\beta^2 r^2]^{\frac{1}{2}}} \right\}$$

so that

$$\frac{\partial\varphi}{\partial x} = \frac{U\tan\theta}{2}\left\{\left[\frac{R-\xi_0\tan\theta+\xi\tan\theta}{[(x-\xi)^2+\beta^2 r^2]^{\frac{1}{2}}}\right]_{\xi_0}^{\xi_1} + \tan\theta\left[\sin h^{-1}\frac{x-\xi}{\beta r}\right]_{\xi_0}^{\xi_1}\right\}.$$

Again

$$C_p = -\frac{2}{U}\frac{\partial\varphi}{\partial x}$$

giving

$$C_p = -\tan\theta\left\{\frac{R-\xi_0\tan\theta+\xi_1\tan\theta}{[(x-\xi_1)^2+\beta^2 r^2]^{\frac{1}{2}}} - \frac{R}{[(x-\xi_0)^2+\beta^2 r^2]^{\frac{1}{2}}}\right\}$$
$$-\tan^2\theta\left\{\sin h^{-1}\left(\frac{x-\xi_1}{\beta r}\right) - \sin h^{-1}\left(\frac{x-\xi_0}{\beta r}\right)\right\}. \qquad \text{(A.5)}$$

A.3. *Sting fairing cap*

In this case $S = \pi[R^2-(\xi_1-\xi)^2]$ (*see* Fig. 48)

and

$$S'(\xi) = 2\pi(\xi_1-\xi)$$

$$\varphi = -\frac{U}{2}\int_{\xi_0}^{\xi_1}\frac{(\xi_1-\xi)}{[(x-\xi)^2+\beta^2 r^2]^{\frac{1}{2}}}\,d\xi$$

and

$$\frac{\partial\varphi}{\partial x} = \frac{U}{2}\left\{\xi_1\int_{\xi_0}^{\xi_1}\frac{\partial}{\partial\xi}\left[\frac{1}{[(x-\xi)^2+\beta^2 r^2]^{\frac{1}{2}}}\right]d\xi - \int_{\xi_0}^{\xi_1}\xi\frac{\partial}{\partial\xi}\left[\frac{1}{[(x-\xi)^2+\beta^2 r^2]^{\frac{1}{2}}}\right]d\xi\right\}$$

therefore

$$\frac{\partial\varphi}{\partial x} = \frac{U}{2}\left\{\xi_1\left[\frac{1}{[(x-\xi)^2+\beta^2 r^2]^{\frac{1}{2}}}\right]_{\xi_0}^{\xi_1} - \left[\frac{\xi}{[(x-\xi)^2+\beta^2 r^2]^{\frac{1}{2}}}\right]_{\xi_0}^{\xi_1} + \int_{\xi_0}^{\xi_1}\frac{d\xi}{[(x-\xi)^2+\beta^2 r^2]^{\frac{1}{2}}}\right\}$$

$$= \frac{U}{2}\left\{\left[\frac{(\xi_1-\xi)}{[(x-\xi)^2+\beta^2 r^2]^{\frac{1}{2}}} - \sin h^{-1}\left(\frac{x-\xi}{\beta r}\right)\right]_{\xi_0}^{\xi_1}\right\}.$$

Since

$$C_p = -\frac{2}{U}\frac{\partial\varphi}{\partial x}$$

we have

$$C_p = \frac{(\xi_1 - \xi_0)}{[(x-\xi_0)^2 + \beta^2 r^2]^{\frac{1}{2}}} + \sin h^{-1}\left(\frac{x-\xi_1}{\beta r}\right) - \sin h^{-1}\left(\frac{x-\xi_0}{\beta r}\right). \tag{A.6}$$

APPENDIX B

Calculation of Blockage Pressure Field of Various Probe Components

Calculations of the blockage pressure fields or blockage velocities, due to a variety of aerodynamic shapes have been published by several authors[6,8]. For example, Thom and Jones[6] have calculated the velocity increments on the centreline and walls of a 10 ft × 7 ft wind tunnel due to a point doublet on the centreline and to a finite span (6 ft) unswept wing represented by a line source-sink combination. Evans[8] has performed extensive calculations of the blockage velocities in a 10 ft × 7 ft tunnel due to a wide range of wings of differing span to tunnel-width ratios and angles of sweep back. In addition he calculated the blockage velocities due to an isolated source on the centreline and at various spanwise positions, again for a 10 ft × 7 ft tunnel. The latter is of more fundamental interest since it enables the blockage of source-sink distributions (wings, bodies, etc.) to be computed from a basic solution.

In the case of a square section tunnel, there are no published calculations of the blockage velocities due to an isolated source on the tunnel centreline. In the present case, then, it is at first necessary to calculate this fundamental solution, i.e. the blockage velocity increment on the tunnel centreline and the total velocity increment (direct + blockage) on the tunnel wall due to an isolated source on the centreline. The derivation although differing only slightly from that of Evans[8] or Thom and Jones[6] is included for completeness.

In order that the walls of the tunnel shall remain stream surfaces, a doubly infinite array of image sources must be assumed (Fig. 49). For a source at $x = y = z = 0$ (x, y and z are distances measured in a Cartesian co ordinate system with origin on the tunnel centreline and x increasing downstream, as shown in Fig. 49), the image sources are located at $x = 0$, $y = Mh$, $z = Nh$, where h is the tunnel height and where M and N can take all integral values between 1 and ∞ (both positive and negative). The calculation of the blockage velocities due to the single source involves the summation of the direct velocities due to the infinite system of image sources.

The perturbation velocity, u, parallel to $0x$, due to a single source at $x = y = z = 0$, in an unbounded incompressible stream, is given by,

$$u = \frac{m}{4\pi} \frac{x}{(x^2+y^2+z^2)^{3/2}}, \tag{B.1}$$

where m is the source strength. Therefore, the blockage perturbation velocity on the tunnel centreline, u_1, due to an infinite array of sources is given by,

$$u_1 = \frac{m}{4\pi} \cdot \sum_{M=-\infty}^{\infty} \sum_{N=-\infty}^{\infty} \frac{x}{(x^2+M^2h^2+N^2h^2)^{3/2}},$$

and excluding $M = N = 0$.

Rearranging we obtain,

$$u_1 = \frac{1}{4\pi}\left(\frac{m}{h^2}\right)\left(\frac{x}{h}\right)\sum_{M=-\infty}^{\infty}\sum_{N=-\infty}^{\infty}\frac{1}{\left[\left(\frac{x}{h}\right)^2+M^2+N^2\right]^{3/2}}. \tag{B.2}$$

The present method involves evaluating the above summation for a finite number of terms (usually 5 to 15), such that the contribution from the remaining terms is small but not insignificant. A correction to the finite sum is then calculated by assuming that the remaining image sources can be replaced by a continuous, uniform, source distribution. For a summation over $-N_1 \leqslant M \leqslant N_1$, $-N_1 \leqslant N \leqslant N_1$, the correction term is given by,

$$\Delta u_1 = 4 \cdot \frac{1}{4\pi}\left(\frac{m}{h^2}\right)\left(\frac{x}{h}\right)\left\{\int_0^{\infty}\int_0^{\infty}\frac{d\left(\frac{y}{h}\right)d\left(\frac{z}{h}\right)}{\left[\left(\frac{x}{h}\right)^2+\left(\frac{y}{h}\right)^2+\left(\frac{z}{h}\right)^2\right]^{3/2}}\right.$$

$$\left. -\int_0^{(Y/h)}\int_0^{(Z/h)}\frac{d\left(\frac{y}{h}\right)d\left(\frac{z}{h}\right)}{\left[\left(\frac{x}{h}\right)^2+\left(\frac{y}{h}\right)^2+\left(\frac{z}{h}\right)^2\right]^{3/2}}\right\},$$

where $\left(\frac{Y}{h}\right) = \left(\frac{Z}{h}\right) = \frac{2N_1+1}{2}$.

Integration with respect to $\left(\frac{y}{h}\right)$ and $\left(\frac{z}{h}\right)$ gives,

$$\Delta u_1 = \frac{1}{\pi}\left(\frac{m}{h^2}\right)\left\{\left[\tan^{-1}\frac{\left(\frac{y}{h}\right)\left(\frac{z}{h}\right)}{\left(\frac{x}{h}\right)\left[\left(\frac{x}{h}\right)^2+\left(\frac{y}{h}\right)^2+\left(\frac{z}{h}\right)^2\right]^{\frac{1}{2}}}\right]_{0\ 0}^{\infty\ \infty}\right.$$

$$\left. -\left[\tan^{-1}\frac{\left(\frac{y}{h}\right)\left(\frac{z}{h}\right)}{\left(\frac{x}{h}\right)\left[\left(\frac{x}{h}\right)^2+\left(\frac{y}{h}\right)^2+\left(\frac{z}{h}\right)^2\right]^{\frac{1}{2}}}\right]_{0\ 0}^{\left(\frac{Y}{h}\right)\left(\frac{Z}{h}\right)}\right\}.$$

Therefore

$$\Delta u_1 = \frac{1}{\pi}\left(\frac{m}{h^2}\right)\left[\frac{\pi}{2}-\tan^{-1}\frac{\left(\frac{Y}{h}\right)\left(\frac{Z}{h}\right)}{\left(\frac{x}{h}\right)\left[\left(\frac{x}{h}\right)^2+\left(\frac{Y}{h}\right)^2+\left(\frac{Z}{h}\right)^2\right]^{\frac{1}{2}}}\right].$$

Substituting for $\left(\frac{Y}{h}\right) = \left(\frac{Z}{h}\right) = \frac{2N_1+1}{2}$, we obtain

$$\Delta u_1 = \frac{1}{\pi}\left(\frac{m}{h^2}\right)\tan^{-1}\left\{\frac{2\left(\frac{x}{h}\right)\left[4\left(\frac{x}{h}\right)^2+2(2N_1+1)^2\right]^{\frac{1}{2}}}{(2N_1+1)^2}\right\}. \tag{B.3}$$

The total perturbation velocity on the tunnel wall (direct and blockage), u_2, due to an infinite array of sources is given by,

$$u_2 = \frac{1}{4\pi}\left(\frac{m}{h^2}\right)\left(\frac{x}{h}\right)\sum_{M=-\infty}^{\infty}\sum_{N=-\infty}^{\infty}\frac{1}{\left[\left(\frac{x}{h}\right)^2+(M+\frac{1}{2})^2+N^2\right]^{3/2}},$$

including $M = N = 0$.

As in the case of the centreline blockage velocity, the above summation is evaluated for a finite number of terms and is then corrected for the difference between the infinite and finite sums. In this case the correction term is given by,

$$\Delta u_2 = 4\times\frac{1}{4\pi}\cdot\left(\frac{m}{h^2}\right)\left(\frac{x}{h}\right)\left\{\int_0^{\infty}\int_0^{\infty}\frac{d\left(\frac{y_1}{h}\right)d\left(\frac{z}{h}\right)}{\left[\left(\frac{x}{h}\right)^2+\left(\frac{y_1}{h}\right)^2+\left(\frac{z}{h}\right)^2\right]^{3/2}}\right.$$

$$\left.-\int_0^{Y_1/h}\int_0^{Z/h}\frac{d\left(\frac{y_1}{h}\right)d\left(\frac{z}{h}\right)}{\left[\left(\frac{x}{h}\right)^2+\left(\frac{y_1}{h}\right)^2+\left(\frac{z}{h}\right)^2\right]^{3/2}}\right\},$$

where

$$\left(\frac{y_1}{h}\right) = \left(\frac{y}{h}\right)+\tfrac{1}{2},$$

$$\left(\frac{Y_1}{h}\right) = N_1+1,$$

$$\left(\frac{Z}{h}\right) = \frac{2N_1+1}{2}.$$

On integration we have,

$$\Delta u_2 = \frac{1}{\pi}\left(\frac{m}{h^2}\right)\left\{\left[\tan^{-1}\frac{\left(\frac{y_1}{h}\right)\left(\frac{z}{h}\right)}{\left(\frac{x}{h}\right)\left[\left(\frac{x}{h}\right)^2+\left(\frac{y_1}{h}\right)^2+\left(\frac{z}{h}\right)^2\right]^{\frac{1}{2}}}\right]_0^{\infty\,\infty}\right.$$

$$\left.-\left[\tan^{-1}\frac{\left(\frac{y_1}{h}\right)\left(\frac{z}{h}\right)}{\left(\frac{x}{h}\right)\left[\left(\frac{x}{h}\right)^2+\left(\frac{y_1}{h}\right)^2+\left(\frac{z}{h}\right)^2\right]^{\frac{1}{2}}}\right]_0^{\left(\frac{Y_1}{h}\right)\left(\frac{Z}{h}\right)}\right\}.$$

Therefore

$$\Delta u_2 = \frac{1}{\pi}\left(\frac{m}{h^2}\right)\left\{\frac{\pi}{2} - \tan^{-1}\frac{\left(\frac{Y_1}{h}\right)\left(\frac{Z}{h}\right)}{\left(\frac{x}{h}\right)\left[\left(\frac{x}{h}\right)^2+\left(\frac{Y_1}{h}\right)^2+\left(\frac{Z}{h}\right)^2\right]^{\frac{1}{2}}}\right\}.$$

Substituting for $\left(\frac{Y_1}{h}\right) = N_1 + 1$, and $\left(\frac{Z}{h}\right) = 2N_1 + 1/2$, we obtain,

$$\Delta u_2 = \frac{1}{\pi}\left(\frac{m}{h^2}\right)\tan^{-1}\left\{\frac{\left(\frac{x}{h}\right)\left[4\left(\frac{x}{h}\right)^2+4(N_1+1)^2+(2N_1+1)^2\right]^{\frac{1}{2}}}{(N_1+1)\ (2N_1+1)}\right\}. \tag{B.5}$$

The asymptotic values of u_1 and u_2 for large values of x can be calculated by the double integration method, used above to calculate the correction terms, except that in this case the integration is performed over the entire yz plane.

It is then found that,

$$u_{1\max} = u_{2\max} = \frac{m}{2h^2}. \tag{B.6}$$

The concept of a single source on the tunnel centreline is unrealistic, in that, we must also add a sink an infinite distance downstream of the source in order that the flow a large distance upstream of the source remains undisturbed. This source-sink combination can be replaced by an appropriate semi-infinite body of revolution, having a cross sectional area S a large distance downstream of the source, where the local stream velocity is higher than free stream velocity by an amount u^*. From mass flow considerations we have,

$$(U+u^*)\ (h^2-S) = Uh^2. \tag{B.7}$$

Expanding the two brackets we obtain,

$$Uh^2 + u^*h^2 - US - u^*S = Uh^2.$$

For bodies which are small compared with the tunnel cross sectional area, u^*S can be ignored, and we are left with,

$$u^*h^2 - US = 0,$$

or

$$u^* = \frac{US}{h^2}. \tag{B.8}$$

Since the entire source flow must be contained by the body cross section, we have,

$$m = US. \tag{B.9}$$

And by comparison with equation (B.6) it is found that

$$u_{1\,\max} = u_{2\,\max} = \frac{u^*}{2}. \tag{B.10}$$

We now define $\Pi_1 = u_1/u^* = C_{p_1}/C_p^*$ and $\Pi_2 = u_2/u^* = C_{p_2}/C_p^*$, and these functions as computed by the method detailed above for an isolated source at $x = 0$ are shown in Fig. 50. The functions are both anti-symmetric, being positive for x positive (downstream of the source). In this figure the incompressible data has been corrected to compressible form by means of Göthert's rule, i.e.

$$C_{p_{\text{compressible}}} = \frac{1}{\beta^2} C_{p_{\text{incompressible}}}(x, \beta y, \beta z),$$

where $\beta = \sqrt{1-M^2}$.

It follows that,

$$C_p^* = -\frac{2u^*}{U} = -\frac{2S}{\beta^2 h^2} = -\frac{2m}{\beta^2 h^2 U}. \tag{B.11}$$

The appropriate expression for the blockage pressure coefficient due to an isolated source at $x = 0$ and a sink at $x = +\infty$ is,

$$\frac{C_p}{C_p^*} = \tfrac{1}{2} + \Pi, \tag{B.12}$$

which tends to zero for x large and negative and to unity for x large and positive.

It is now possible to calculate the blockage pressure distribution due to a continuous distribution of sources along the tunnel centreline. The blockage pressure coefficient in this case is given by,

$$\Delta C_{p(x)} = \int_{\xi_0}^{\xi_1} \frac{\partial C_p}{\partial C_p^*} \cdot \frac{\partial C_p^*}{\partial m} \cdot \frac{\partial m}{\partial \xi} \cdot d\xi, \tag{B.13}$$

where

$$\frac{\partial C_p}{\partial C_p^*} = \tfrac{1}{2} + \Pi_1\left(\frac{x-\xi}{\beta h}\right) \quad \text{on the tunnel centreline,}$$

and

$$= \tfrac{1}{2} + \Pi_2\left(\frac{x-\xi}{\beta h}\right) \quad \text{on the tunnel wall.}$$

$$\frac{\partial C_p^*}{\partial m} = -\frac{2}{\beta^2 h^2 U}$$

and

$$\frac{\partial m}{\partial \xi} = U \frac{\partial S}{\partial \xi}.$$

Since we are dealing with bodies of revolution,

$$S(\xi) = \pi R^2 \text{ and } \frac{\partial S}{\partial \xi} = 2\pi R \frac{\partial R}{\partial \xi}$$

where R is the body radius at ξ.
Substituting for $\partial C_p/\partial C_p^*$, $\partial C_p^*/\partial m$ and $\partial m/\partial \xi$ in equation (B.13) we obtain,

$$-\Delta C_{p(x)} = \frac{4\pi}{\beta^2 h^2} \int_{\xi_0}^{\xi_1} R \frac{\partial R}{\partial \xi} \left\{ \tfrac{1}{2} + \Pi\left(\frac{x-\xi}{\beta h} \right) \right\} d\xi , \tag{B.14}$$

which can be re-written as,

$$-\Delta C_{p(x)} = \frac{2\pi}{\beta^2 h^2} \int_{R_0}^{R_1} \left\{ \tfrac{1}{2} + \Pi\left(\frac{x-\xi}{\beta h} \right) \right\} d(R^2)$$

$$= \frac{\pi}{\beta^2 h^2} \left[R_1^2 - R_0^2 \right] + \frac{2\pi}{\beta^2 h^2} \int_{R_0}^{R_1} \Pi\left(\frac{x-\xi}{\beta h} \right) d(R^2) .$$

The integral may be approximated by a $2n+1$ repeated Simpson sum, and evaluated numerically, i.e.

$$\int_{R_0}^{R_1} \Pi\left(\frac{x-\xi}{\beta h} \right) d(R^2) = \sum_{j=0}^{2n} \begin{pmatrix} 1 \\ 4 \\ 2 \end{pmatrix} \left[\Pi\left(\frac{x-\xi_j}{\beta h} \right) \right] \left[\frac{R_1^2 - R_0^2}{6n} \right] ,$$

where ξ_j are the points at which

$$R^2 = R_j^2 = R_0^2 + j . \frac{(R_1^2 - R_0^2)}{2n} .$$

Thus

$$-\Delta C_{p(x)} = \frac{\pi}{\beta^2 h^2} [R_1^2 - R_0^2] \left[1 + \frac{1}{3n} \sum_{j=0}^{2n} \begin{pmatrix} 1 \\ 4 \\ 2 \end{pmatrix} \Pi\left(\frac{x-\xi_j}{\beta h} \right) \right] . \tag{B.15}$$

In the present case sufficient accuracy was obtained by approximating each of the various probe components by a 3 point Simpson.

APPENDIX C

Analysis of Tunnel Wall Pressures to Yield the Complete Pressure Field of the Probe Nose and Probe Flare.

Let each wall pressure hole have an identifying number $j, j = 1$ to 12, and let its location relative to the tunnel datum be x_j. The location of the probe datum relative to the tunnel datum at each probe position for which tunnel wall pressures were recorded is x_i, $i = 1$ to 4. With the probe datum at x_i, the static pressure at wall hole j is $(p_j)_i$.

Now define

$$\delta(p_j)_i = (p_j)_i - (p_j)_{i-1},$$

where i is now restricted to $i = 2$ to 4.

Also define

$$[\Delta(p_j)_i]_i = [\delta(p_j)_i]_i - [\delta(p_j)_i]_{i=1}$$

where i is again restricted to $i = 2$ to 4 except where specified as unity.

Assume that for the case $j = 1$ (56 top), $i = 1$ ($x_j = -61$ inches, $x_i = +19$ inches)

$$\delta(p_j)_i = 0.$$

From static pressure measurements at wall hole $j = 1$, $\Delta(p_j)_i$ can be calculated and plotted against $(x_j - x_i)$. Knowing $(x_j - x_i)$ for $j = 2$ and $i = 1$, a value for $\delta(p_j)_i$, $(j = 2, i = 1)$, can be read from the plot of $\Delta(p_j)_i$ against $(x_j - x_i)$, $(j = 1)$. Knowing $\delta(p_j)_i$, $(j = 2, i = 1)$, $\Delta(p_j)_i$, $(j = 2)$ can be calculated from static pressure measurements at wall hole, $j = 2$, and plotted on the same graph as for $\Delta(p_j)_{i=1}$. This procedure repeated for $j = 1$ to 12 will yield the pressure distribution at the tunnel wall due to the probe nose and probe sting flare (Fig. 15). It should be noted that, in reading values of $\delta(p_j)_i$ from the plot of $\Delta(p_j)_i$ against $(x_j - x_i)$, errors are cumulative, but with care these can be kept small. The assumption that $\delta(p_j)_i = 0$ for $j = i = 1$ (56 top) is justified in that linear theory predicts zero pressure difference under these conditions (Fig. 15).

TABLE 1

Details of Supersonic Diffuser Jack Displacements for Tunnel Choked Conditions

Nominal Mach No.	Jack No. 1 movement (inches)	Jack No. 2 movement (inches)	Jack No. 1 tape holes	Jack No. 2 tape holes
1·00	0	0	0	0
0·98	8·600	4·300	1720	860
0·97	8·655	4·325	1731	865
0·96	8·720	4·360	1744	872
0·95	8·790	4·395	1758	879
0·94	8·870	4·435	1774	887
0·93	8·960	4·480	1792	896
0·92	9·055	4·530	1811	905
0·91	9·160	4·580	1832	916
0·90	9·275	4·640	1855	927
0·89	9·395	4·700	1879	939
0·88	9·525	4·760	1905	952
0·87	9·665	4·835	1933	966
0·86	9·810	4·905	1962	981
0·85	9·965	4·985	1993	996
0·84	10·130	5·065	2026	1013
0·83	10·300	5·150	2060	1030
0·82	10·480	5·240	2096	1048
0·81	10·670	5·335	2134	1067
0·80	10·865	5·435	2173	1086
0·79	11·070	5·535	2214	1107
0·78	11·285	5·645	2257	1128
0·77	11·505	5·750	2301	1150
0·76	11·735	5·870	2347	1173
0·75	11·975	5·990	2395	1197
0·74	12·220	6·110	2444	1222
0·73	12·475	6·240	2495	1247
0·72	12·740	6·370	2548	1274
0·71	13·010	6·505	2602	1301
0·70	13·290	6·645	2658	1329
0·69	13·580	6·790	2716	1358
0·68	13·875	6·935	2775	1387
0·67	14·180	7·090	2836	1418
0·66	14·490	7·245	2898	1449
0·65	14·810	7·405	2962	1481
0·64	15·140	7·570	3028	1514
0·63	15·475	7·740	3095	1547
0·62	15·815	7·910	3163	1581
0·61	16·165	8·085	3233	1616
0·60	16·525	8·260	3305	1652

TABLE 2

4-Stage Compressor Speed in rpm at Various Tunnel Total Pressures (tunnel unchoked)

Tunnel total press "Hg	20	40	60	80	100	115
Mach No.						
0·20	189	187	185	183	180	178
0·30	273	270	268	265	263	261
0·40	354	352	349	347	344	342
0·50	427	423	421	418	415	413
0·55	458	455	452	449	446	444
0·60	483	480	477	474	471	
0·65	513	509	505	501		
0·70	536	533	530	527		
0·80	585	582	578			

TABLE 3

Details of Wall Static Holes in 8 ft × 8 ft Wind Tunnel

Wall hole No.				Distance upstream from datum	Tunnel cross section area (sq ft)	Notes
Port	Top	Bottom	Stbd			
Settling chamber and contraction						
1	1	1		105′ 6″	997	
2	2	2		102′ 6″	994	
3	3	3		99′ 6″	984	
4	4	4		96′ 6″	955	
5	5	5		93′ 6″	908	
6	6	6		90′ 6″	842	
7	7	7		87′ 6″	759	
8				83′ 6″	634	
9				79′ 6″	505	
10				75′ 6″	385	
11				71′ 6″	286	
12				67′ 6″	212	
13				64′ 0″	167	
Nozzle and working section						
15				56′ 0″	103·4	
16				52′ 0″	85·2	
17				49′ 0″	76·6	
18				46′ 0″	70·6	
19				43′ 0″	66·6	
20				41′ 0″	64·83	
21				39′ 0″	63·69	
22				37′ 0″	63·02	
23				35′ 0″	62·71	
24				33′ 0″	62·61	
25				31′ 0″	62·63	
26				29′ 6″	62·71	
27				28′ 0″	62·81	
28				26′ 0″	62·97	
29				24′ 6″	63·09	
30				23′ 0″	63·19	
31				21′ 6″	63·28	Subsonic
32*				20′ 6″	63·33	Ref. static
33				19′ 0″	63·40	
34				18′ 0″	63·44	
35				17′ 0″	63·47	
36				16′ 0″	63·51	
37				15′ 1″	63·55	
38				14′ 0″	63·59	
39				13′ 3″	63·62	
40				12′ 6″	63·65	

TABLE 3—*continued*

Details of Wall Static Holes in 8 ft × 8 ft Wind Tunnel

Wall hole No.				Distance upstream from datum	Tunnel cross section area (sq ft)	Notes
Port	Top	Bottom	Stbd			
Nozzle and working section (Contd)						
41				12′ 0″	63·67	
42				11′ 3″	63·70	
43				10′ 6″	63·73	
44				9′ 9″	63·76	
45				9′ 3″	63·78	
46				8′ 9″	63·80	
47				8′ 3″	63·82	
48				7′ 9″	63·84	
49				7′ 3″	63·86	
50				6′ 6″	63·89	
51				6′ 0″	63·90	Supersonic Ref. static
52				5′ 3″	63·93	
	56	56		5′ 1″	63·94	
53				4′ 9″	63·95	
54				4′ 3″	63·97	
	57	57		3′ 7″	63·99	
55				3′ 6″	64·00	
	58*	58*		2′ 7″	64·02	
	59*	59*		1′ 7″	64·06	Holes 60–62 covered by backing plates
	63*	63*		1′ 0½″	64·08	Holes 64–66 covered by backing plates
	67*	67*		0′ 6″	64·09	
	68*	68*		−0′ 6″	64·13	
	69	69		−1′ 0″	64·15	
	70	70		−1′ 6″	64·17	
	71	71		−2′ 0″	64·19	
	72	72		−2′ 6″	64·20	
	73	73		−3′ 0″	64·22	

Tunnel datum is schlieren window centreline (quadrant centre of rotation)
*Indicates that hole has had steel insert fitted (*see* Section 5).

TABLE 3—*continued*

Details of Wall Static Holes in 8 ft × 8 ft Wind Tunnel

Wall hole No.				Distance upstream from datum	
Port	Top	Bottom	Stbd		
Supersonic diffuser					
200				−5′ 6″	
201			201	−6′ 6″	1st Panel
202				−7′ 9″	
203				−9′ 0″	
204				−10′ 6″	
205			205	−12′ 0″	
206				−13′ 9″	
207				−15′ 9″	
208			208	−18′ 3″	2nd Panel
209				−20′ 9″	
210				−23′ 3″	
211			211	−25′ 9″	
212				−28′ 3″	
213				−31′ 9″	
214			214	2′ 4″	On injection doors distances
215			215	0′ 10″	from slot exit hinge
216			216	−36′ 9″	
217				−38′ 9″	
218				−40′ 9″	
219				−42′ 9″	
220				−45′ 3″	3′ 0″ below C_L
221				−45′ 3″	1′ 6″ below C_L 3rd Panel
222			222	−45′ 3″	on C_L
223				−45′ 3″	1′ 6″ above C_L
224				−45′ 3″	3′ 0″ above C_L
225				−49′ 3″	
226			226	−51′ 3″	
227				−53′ 3″	4th Panel
228				−55′ 3″	
229			229	−57′ 3″	
230				−61′ 6″	0′ 6″ above C_L on sliding plate
Subsonic diffuser					
				−68′ 0″	

NOTE: Distances in supersonic diffuser are measured along the wall surface and are merely nominal with reference to tunnel datum.

TABLE 4

Nozzle Geometry, $M = 1{\cdot}00$

Jack No.	x	y Original nozzle	Additional No. of steps	Δy	y Modified nozzle
Slide	4·009	86·406			
2	4·374	85·095			
3	32·483	74·614			
4	61·322	66·349			Identical
5	90·684	60·195			to
6	120·338	55·654			original
7	150·152	52·320			nozzle
8	180·058	49·938			
9	204·022	48·629			
10	228·006	47·767			
11	252·001	47·266			
12	276·000	47·029			
13	300	46·956			
14	321	46·961	2	0·005	46·966
15	342	46·998	13	0·032	47·030
16	363	47·054	28	0·070	47·124
17	384	47·117	45	0·112	47·229
18	405	47·184	59	0·147	47·331
19	426	47·251	66	0·164	47·415
20	447	47·319	68	0·169	47·488
21	468	47·387	64	0·159	47·546
22	489	47·454	59	0·147	47·601
23	510	47·521	105	0·131	47·652
24	531	47·587	94	0·117	47·704
25	552	47·652	82	0·103	47·755
26	576	47·725	69	0·086	47·811
27	600	47·797	58	0·073	47·870
28	624	47·867	46	0·058	47·925
29	648	47·936	35	0·044	47·980
30	672	48·003	25	0·031	48·034
31	696	48·068	16	0·020	48·088
Hinge	744	48·192	0	0	48·192

Date for original nozzle obtained from Ref. 4.
x dimension in inches downstream from working-section datum (Fig. 1).
Jack No. 31 located on schlieren window centreline.
y dimension in inches from tunnel centreline.
Step size 0·00250 inch for jacks 2 to 22.
Step size 0·00125 inch for jacks 23 to 31.

TABLE 5

Working Section Mach Numbers obtained with the Tunnel Choked

M_{nominal}	$R/l = 3{\cdot}0 \times 10^6$ per ft		$R/l = 6{\cdot}0 \times 10^6$ per ft	
	M_{32}	M_{C_L}	M_{32}	M_{C_L}
0·60	0·595	0·596	0·594	0·595
0·65	0·644	0·645	0·644	0·644
0·70	0·693	0·695	0·691	0·692
0·74	0·733	0·735	0·733	0·733
0·78	0·773	0·776	0·774	0·775
0·82	0·813	0·816	0·815	0·815
0·86	0·852	0·857	0·852	0·853
0·90	0·885	0·890	0·888	0·889

M_{32}–Mach number at subsonic reference static hole, No. 32.

M_{C_L}–Mach number at centre of rotation of quadrant on tunnel centreline.

TABLE 6

Static Pressure Distribution along Centreline and Centre of Wall of a Square Tunnel due to a Source on the Centreline

$x/\beta h$	C_{p_1}/C_p^*	C_{p_2}/C_p^*
1/10	0·0713	0·1783
1/6	0·1171	0·2772
1/4	0·1709	0·3688
3/8	0·2419	0·4470
1/2	0·2998	0·4803
3/4	0·3795	0·4978
1	0·4245	0·4997
5/4	0·4502	
3/2	0·4651	
5/2	0·4878	
∞	0·5000	0·5000

$$\left\{\frac{\partial\left[\frac{C_{p_1}}{C_p^*}\right]}{\partial\left[\frac{x}{\beta h}\right]}\right\}_{x=0} = 0{\cdot}716 \qquad \left\{\frac{\partial\left[\frac{C_{p_2}}{C_p^*}\right]}{\partial\left[\frac{x}{\beta h}\right]}\right\}_{x=0} = 1{\cdot}862$$

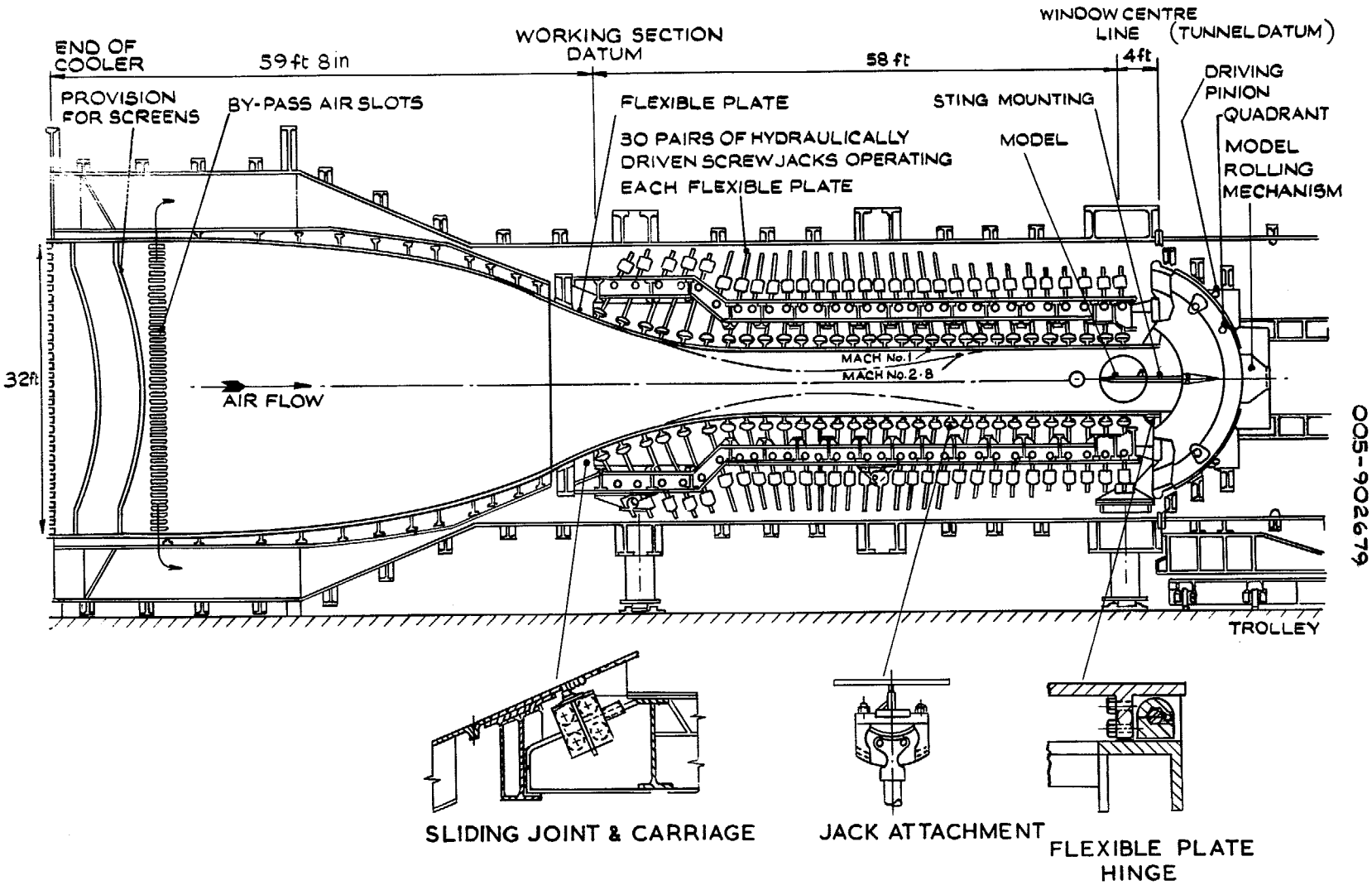

FIG. 1. General arrangement of working section and contraction 8 ft × 8 ft wind tunnel.

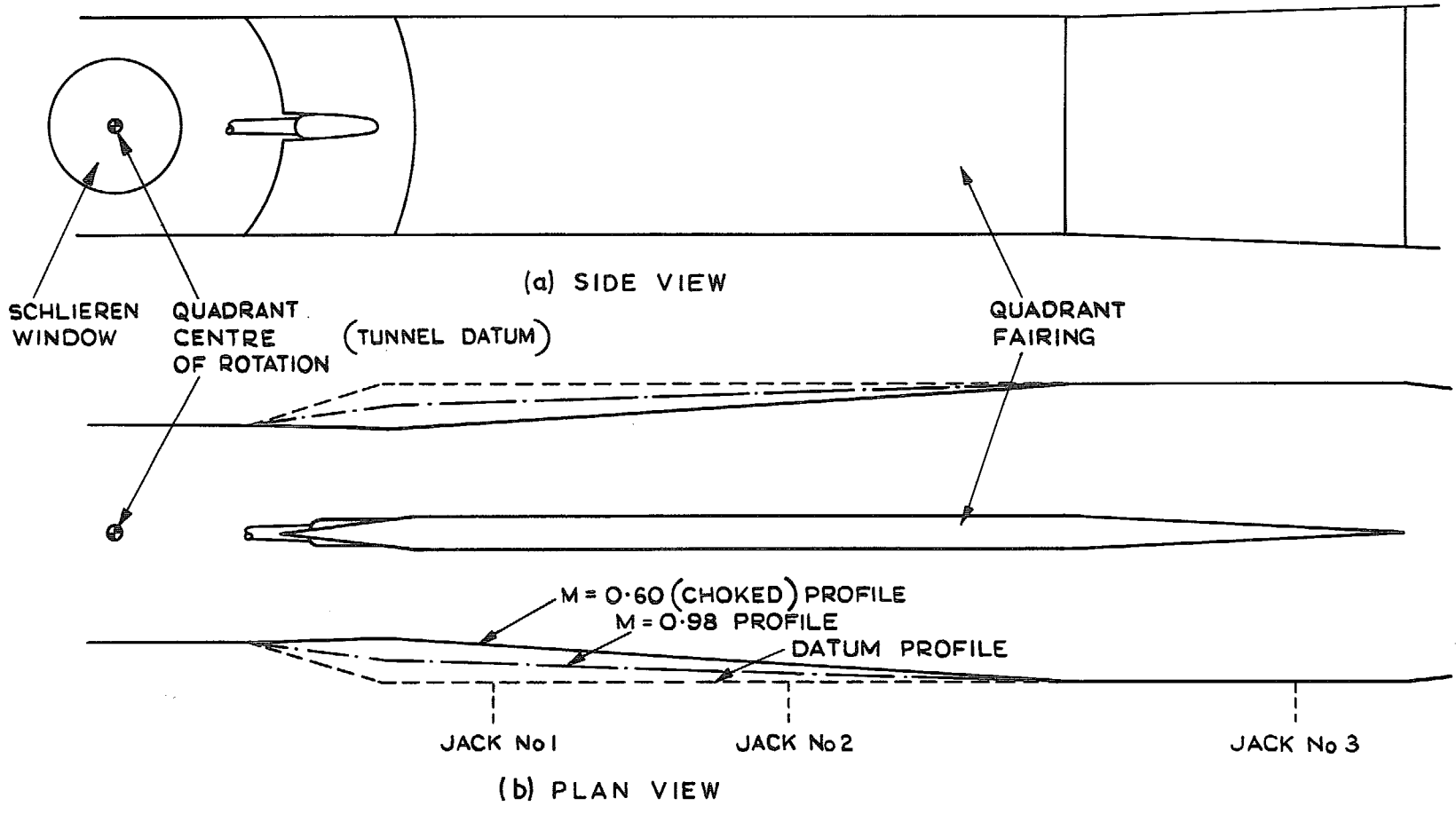

FIG. 2a & b. Layout of supersonic diffuser showing method of choking flow.

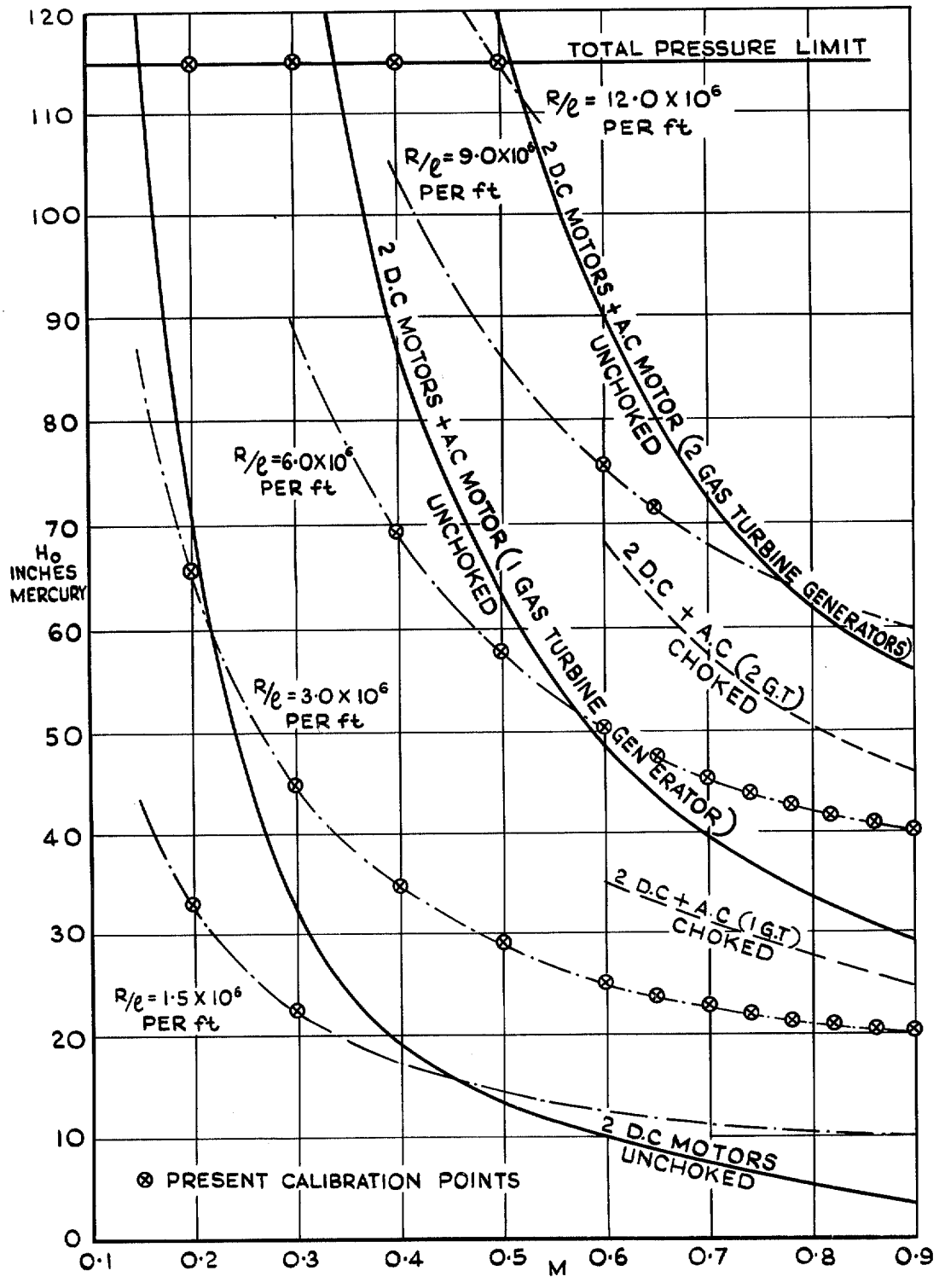

FIG. 3. Performance curves for 8 ft × 8 ft wind tunnel at subsonic speeds with 4-stage compressor and variable frequency a.c. supply.

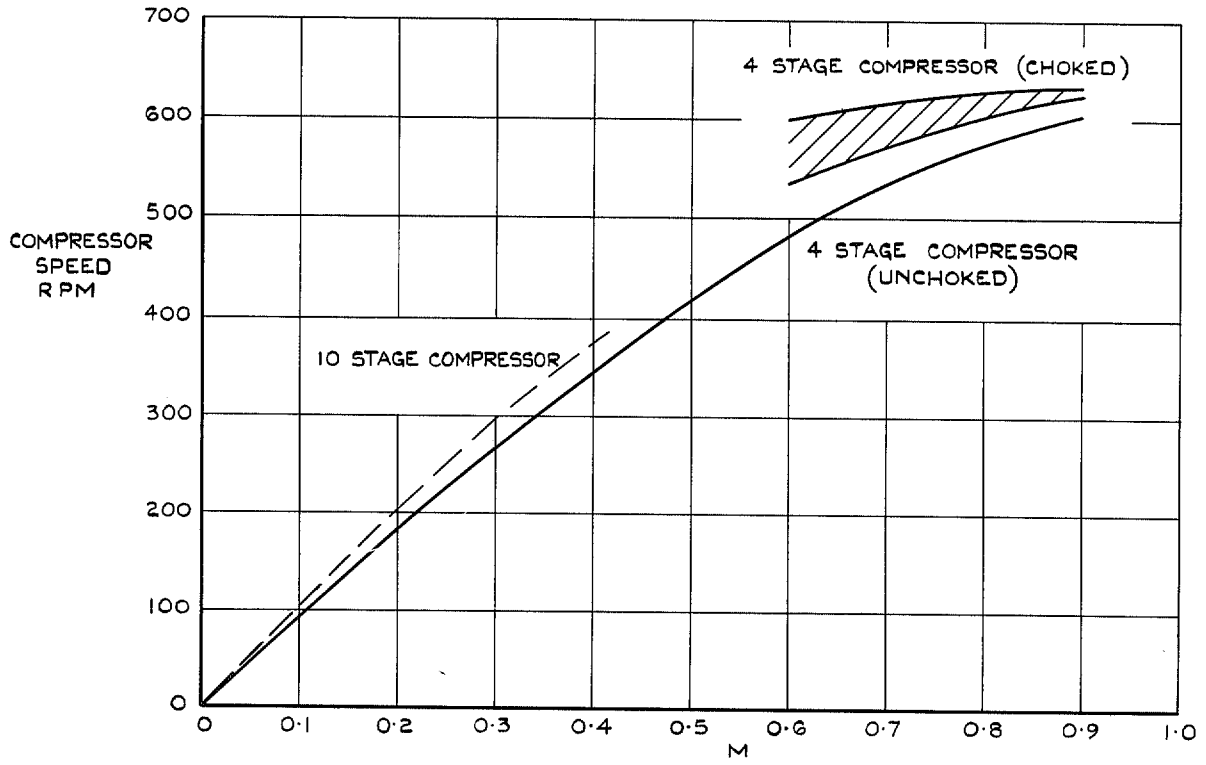

FIG. 4. Variation of compressor speed with Mach number.

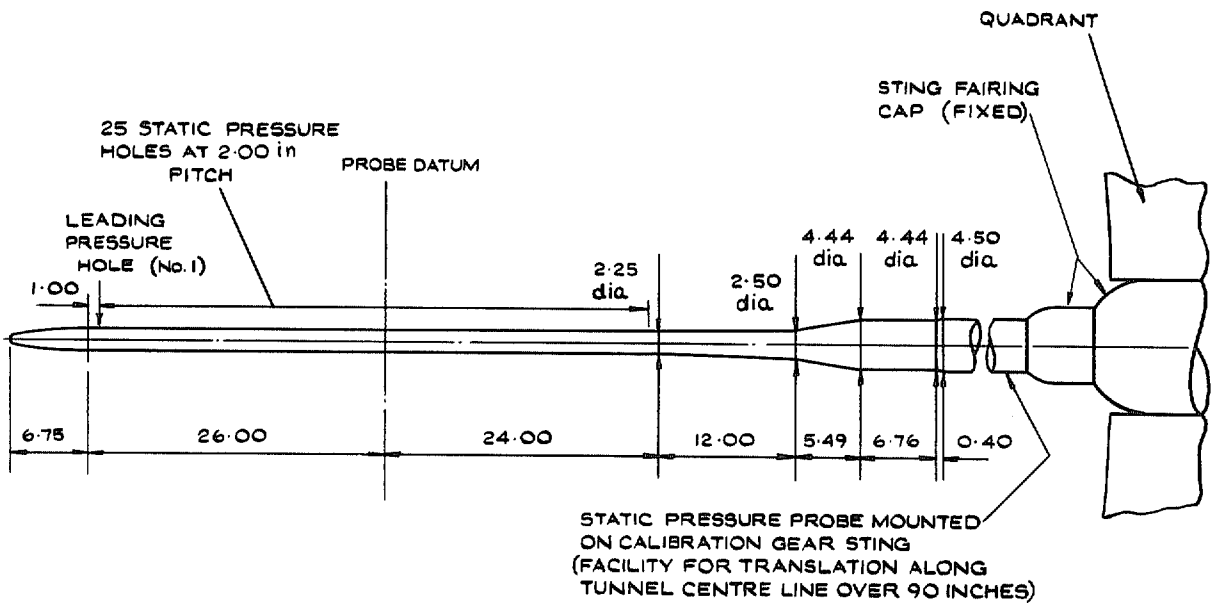

FIG. 5. Subsonic static-pressure probe.

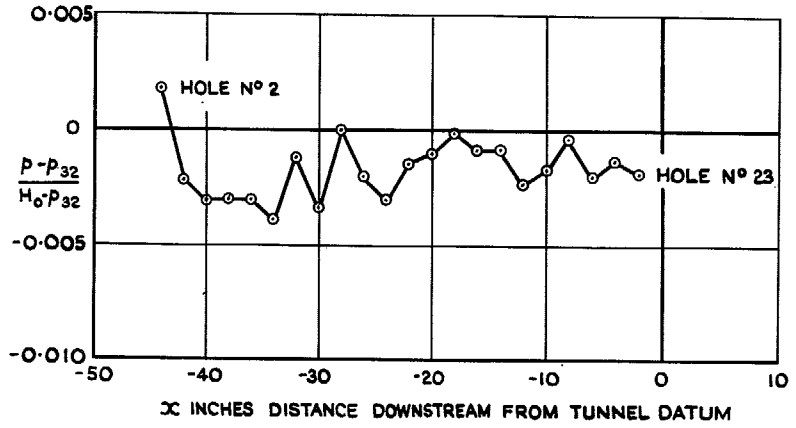

(a) PROBE DATUM 21in UPSTREAM OF TUNNEL DATUM

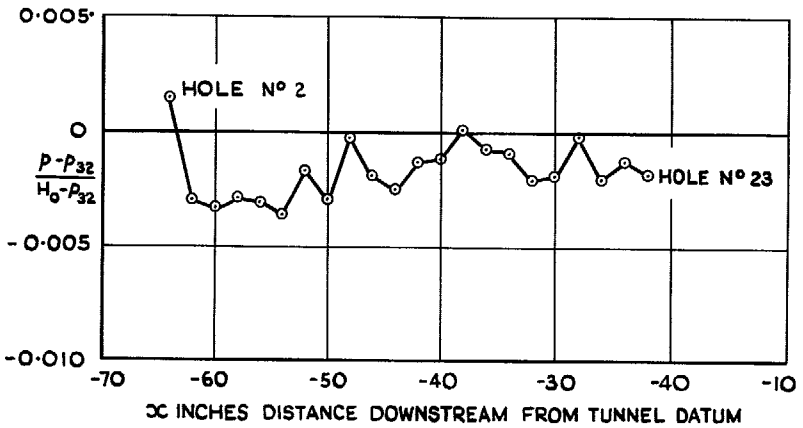

(b) PROBE DATUM 41in UPSTREAM OF TUNNEL DATUM

FIG. 6a & b. Typical pressure distributions along probe at two locations on tunnel centreline, $M = 0{\cdot}74$ (choked), $R/l = 6{\cdot}0 \times 10^6$ per ft.

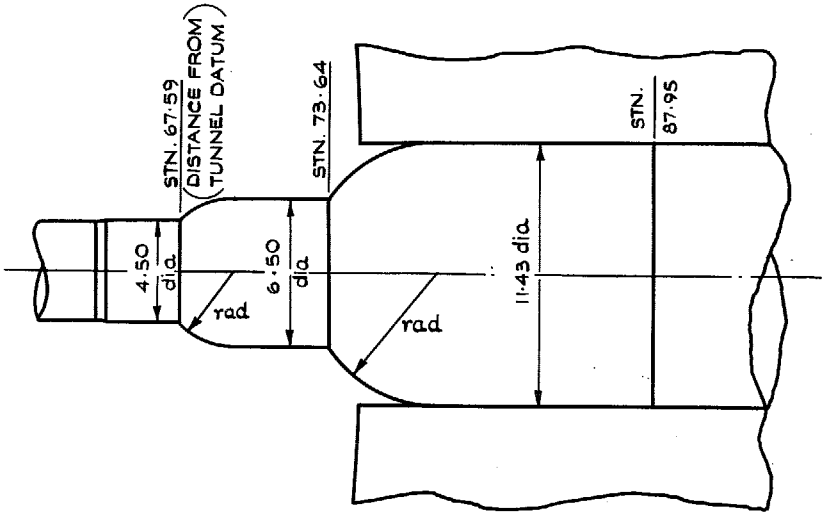

(a) CALIBRATION STING

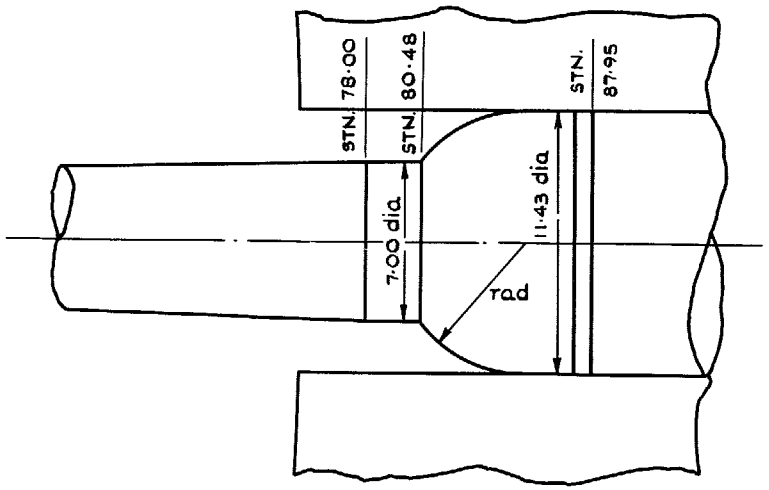

(b) TYPICAL MODEL SUPPORT REAR STING

FIG. 7a & b. Comparison of sting fairing caps on calibration sting and typical model support rear sting.

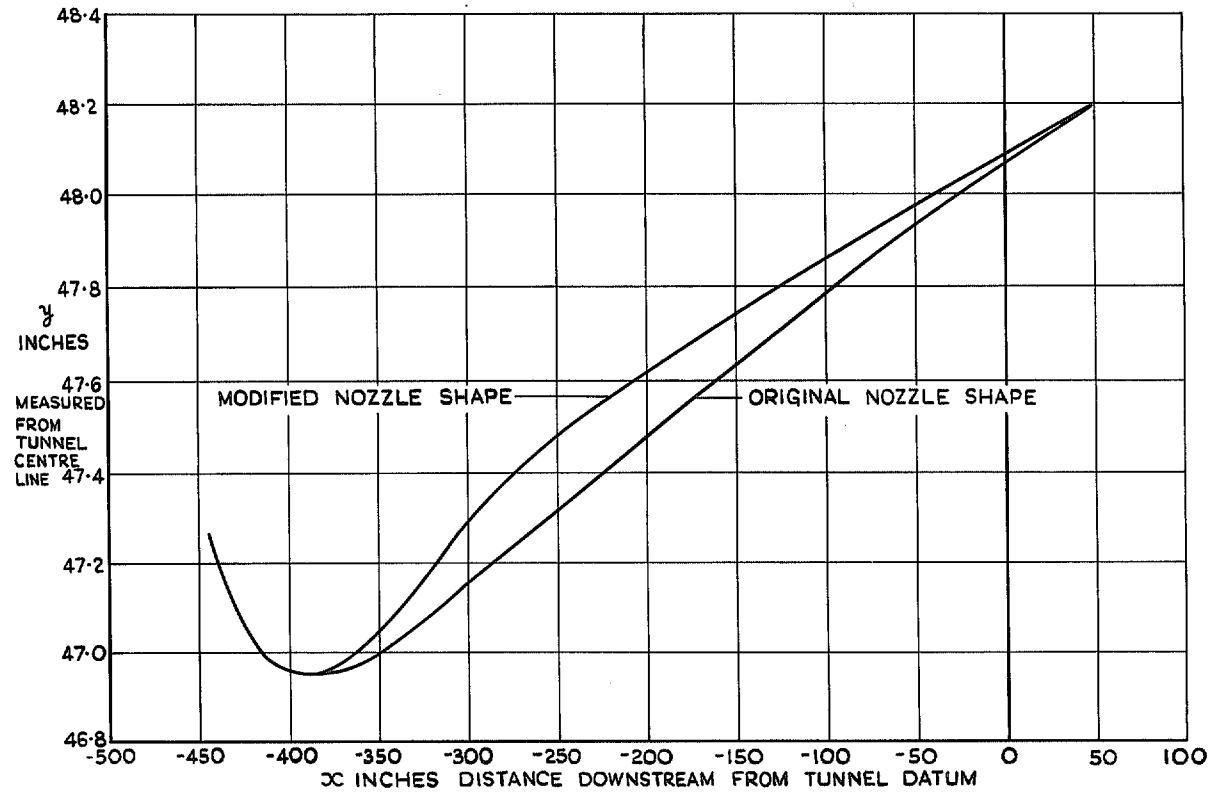

FIG. 8. Comparison between original and modified nozzle shapes.

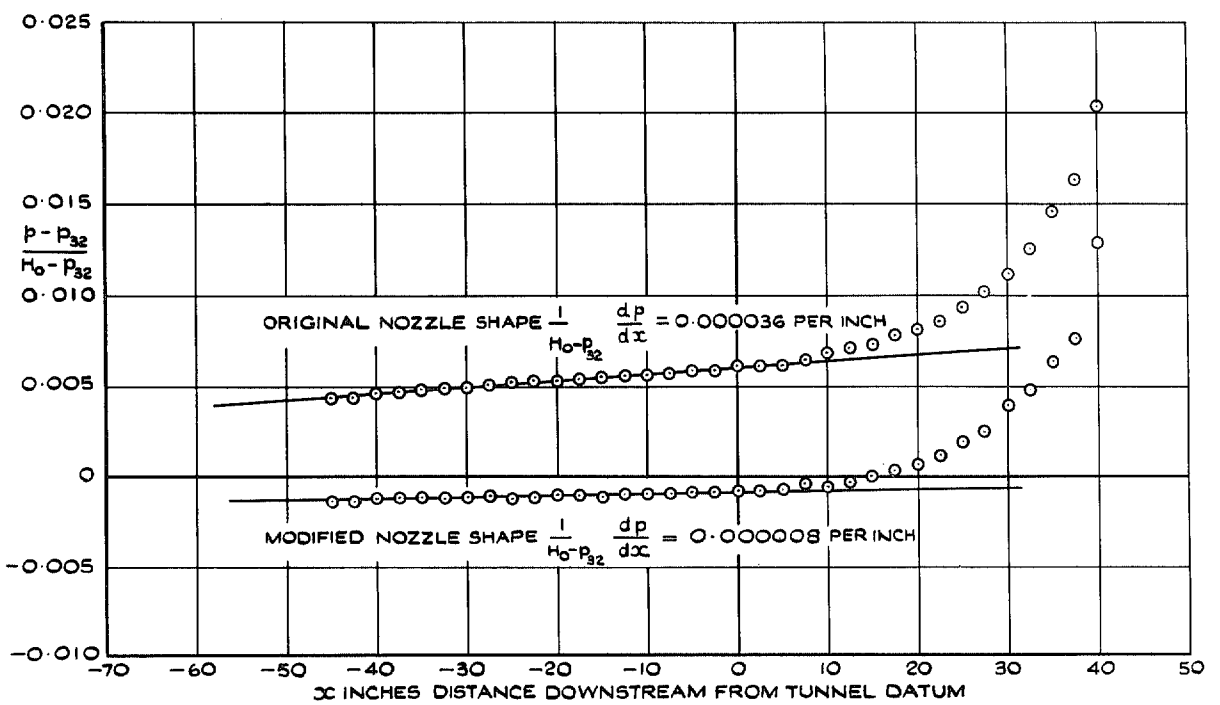

FIG. 9. Effect of modified nozzle shape on working-section pressure gradient.

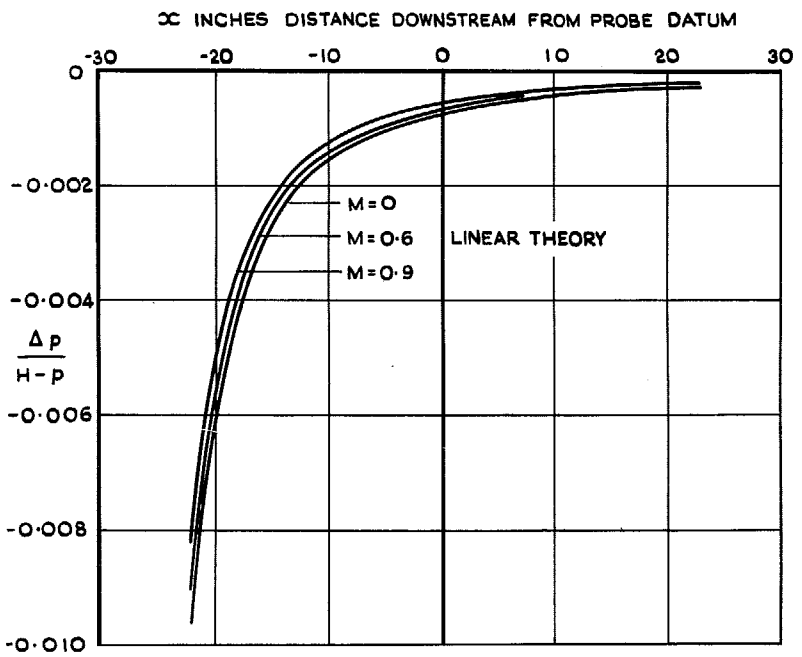

FIG. 10. Direct pressure distribution on tunnel centreline due to probe nose.

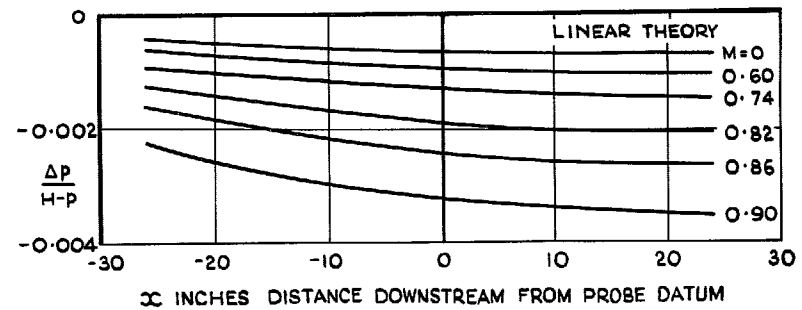

FIG. 11. Blockage pressure distribution on tunnel centreline due to probe nose.

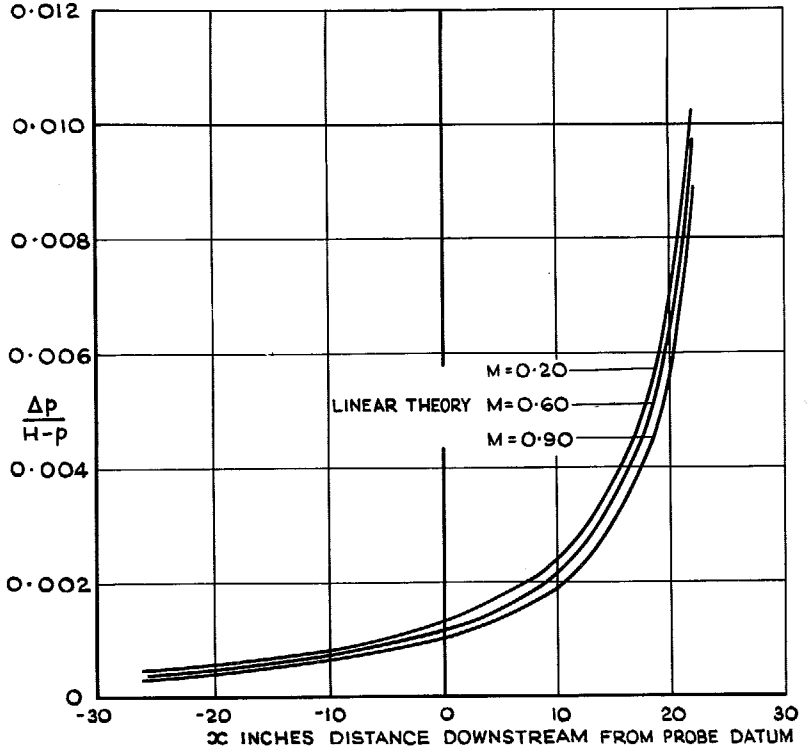

FIG. 12. Direct pressure distribution on tunnel centreline due to probe sting flare.

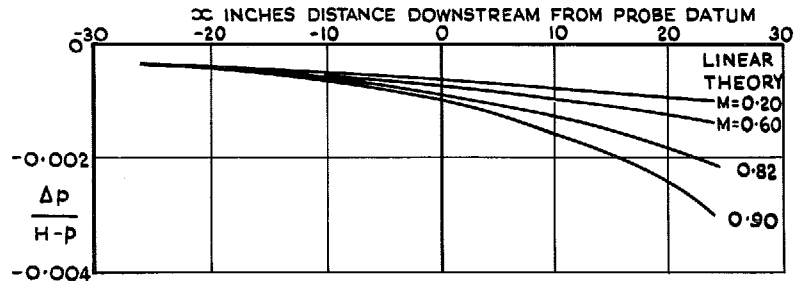

FIG. 13. Blockage pressure distribution on tunnel centreline due to probe sting flare.

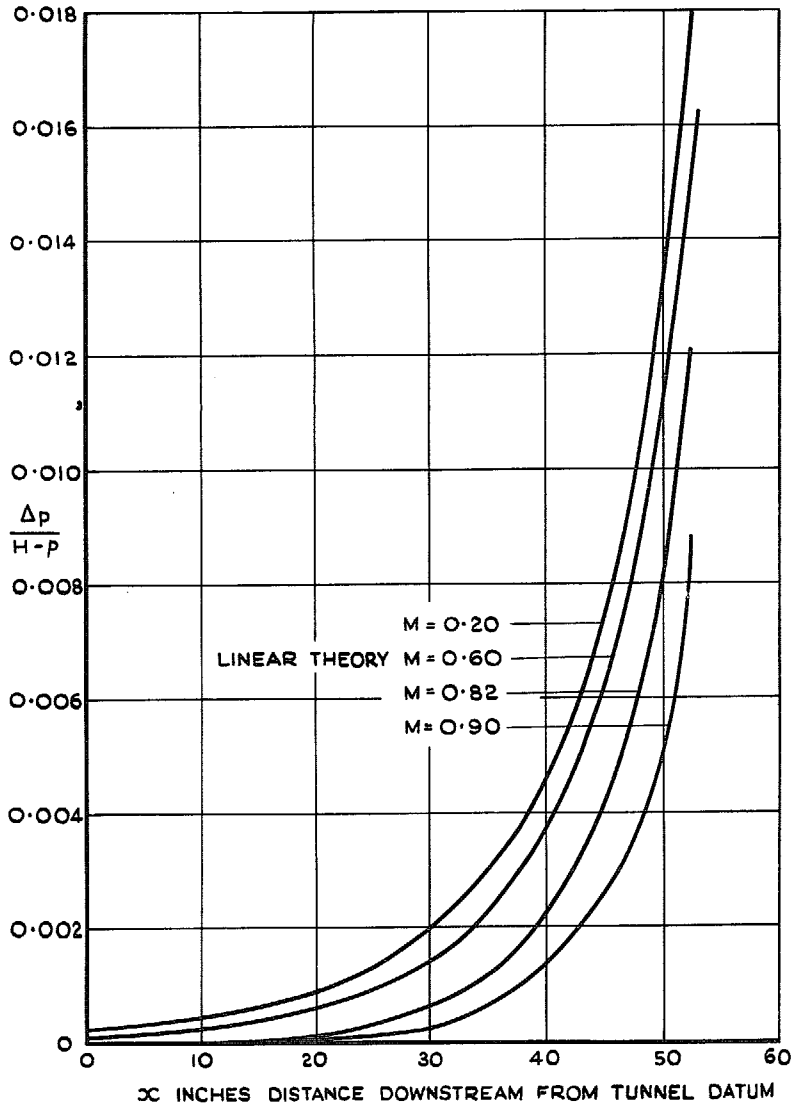

FIG. 14. Pressure distribution (direct + blockage) on tunnel centreline due to difference in sting fairing caps.

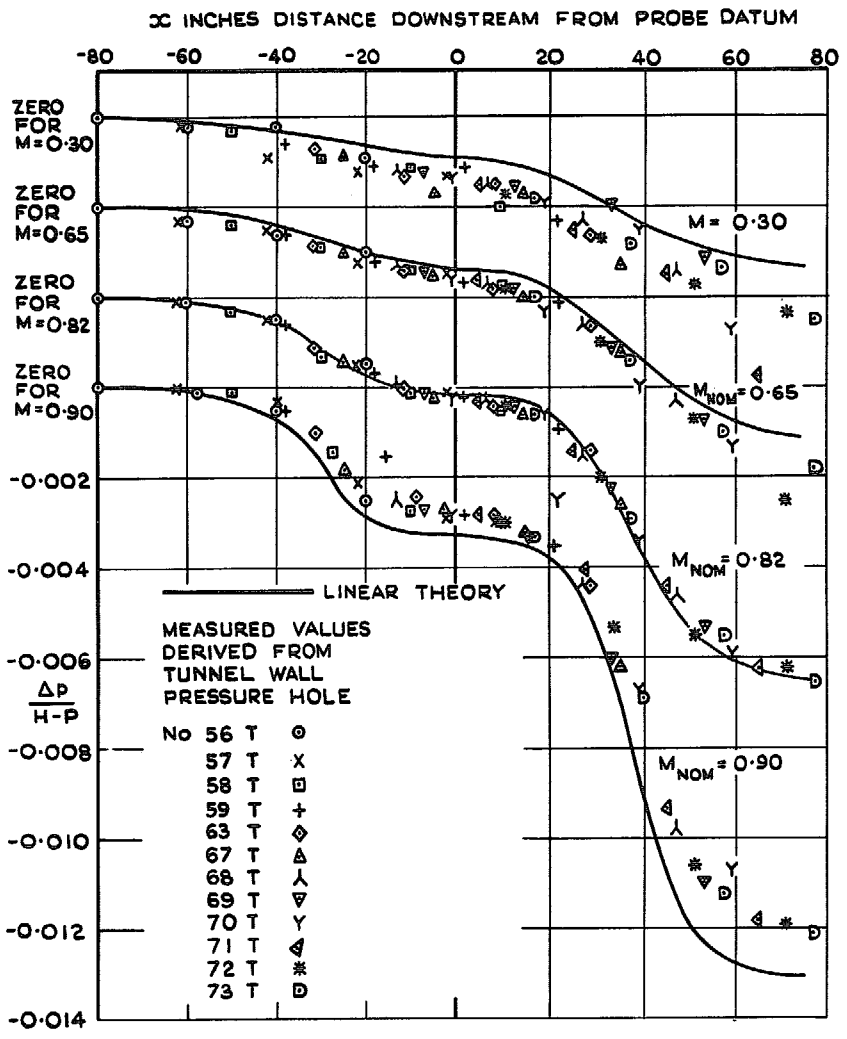

FIG. 15. Pressure distribution (direct + blockage) on tunnel walls due to probe nose and probe sting flare.

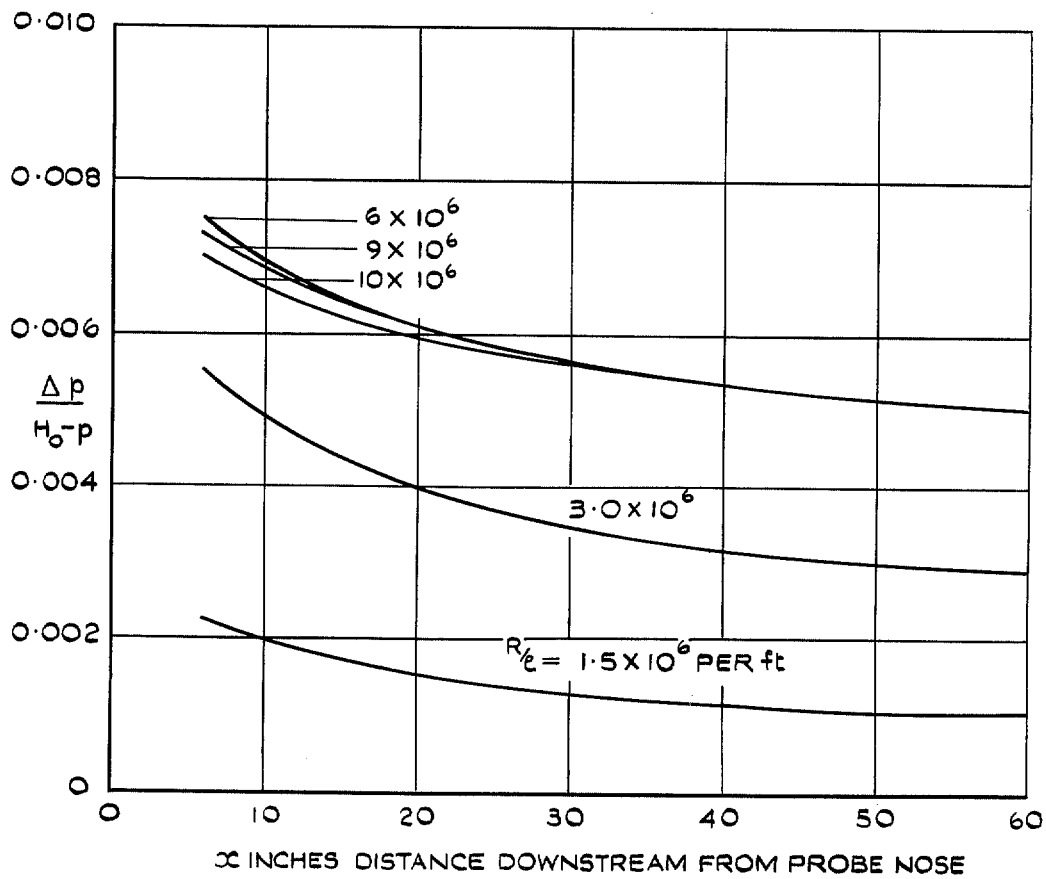

FIG. 16. Variation of error in static-pressure measurement due to hole size with location along probe.

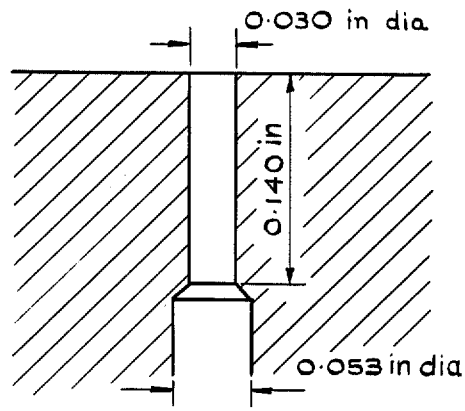

FIG. 17. Details of probe static-pressure holes.

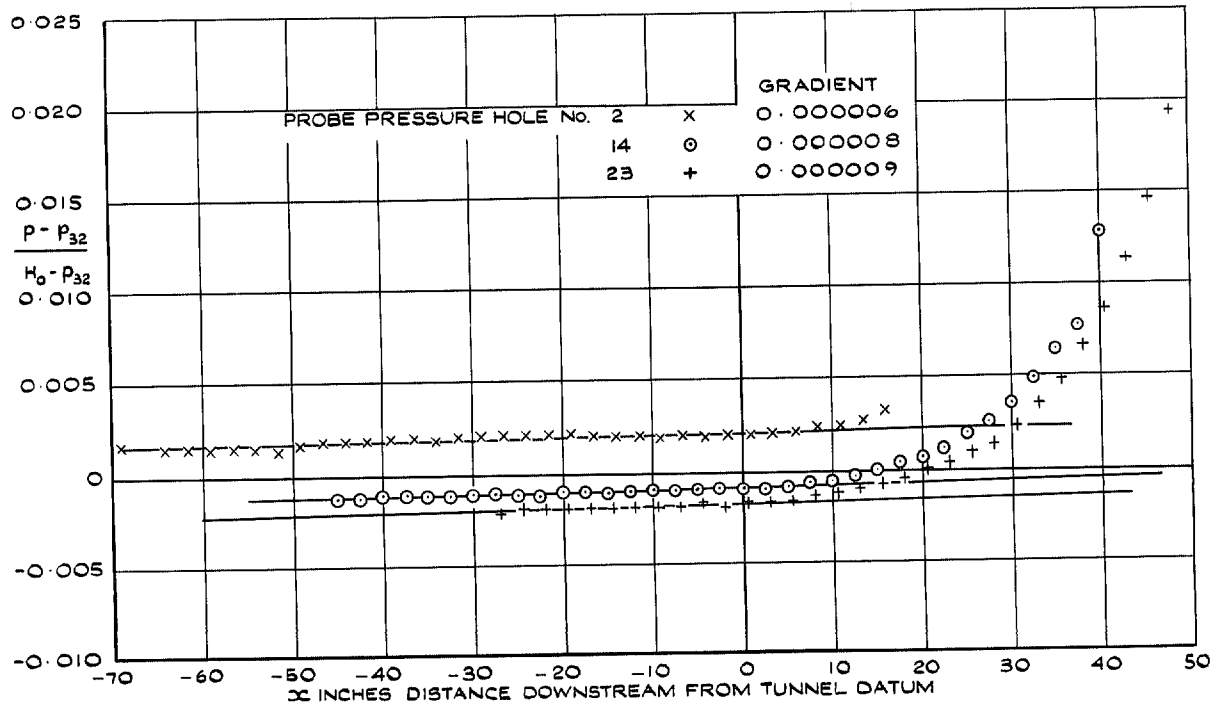

FIG. 18. Typical pressure distributions along tunnel centreline as measured by 3 probe pressure holes. $M = 0{\cdot}74$ (choked), $R/l = 6{\cdot}0 \times 10^6$ per ft.

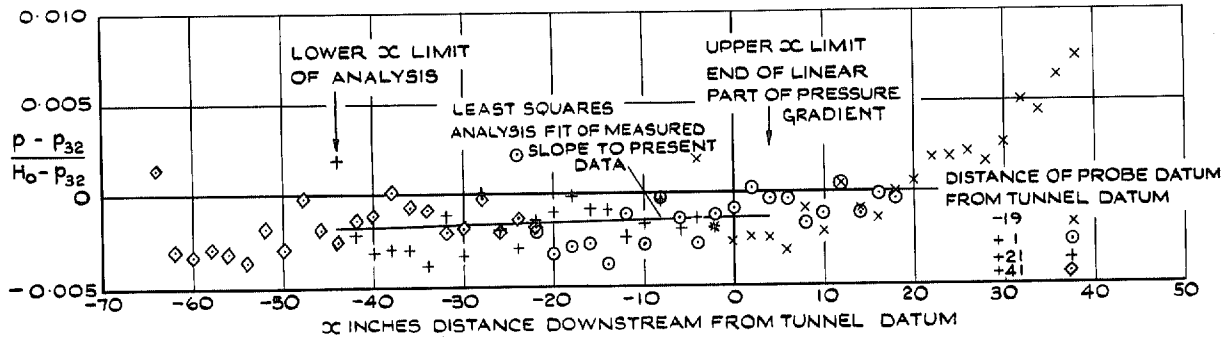

FIG. 19. Typical pressure distributions along probe for 4 probe locations (used in the analysis to establish level of static pressure at tunnel datum) $M = 0{\cdot}74$ (choked), $R/l = 6{\cdot}0 \times 10^6$ per ft.

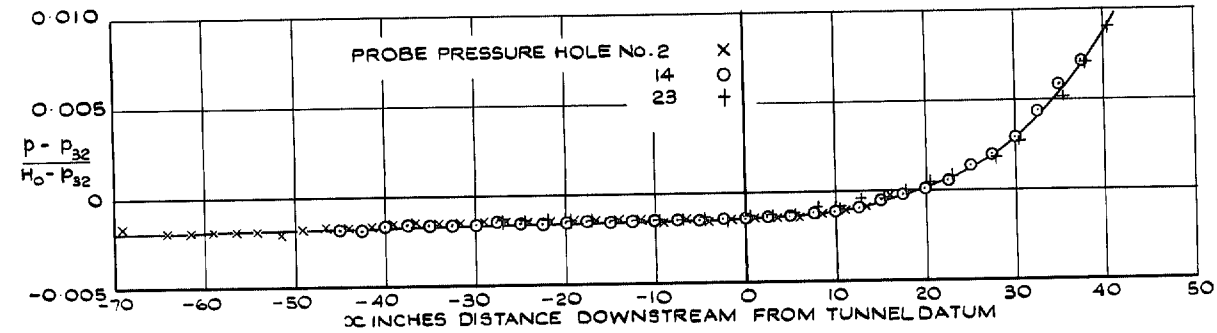

FIG. 20. Typical pressure distributions along tunnel centreline as measured by probe pressure holes. Corrected to static pressure level shown in Fig. 19. $M = 0{\cdot}74$ (choked), $R/l = 6{\cdot}0 \times 10^6$ per ft.

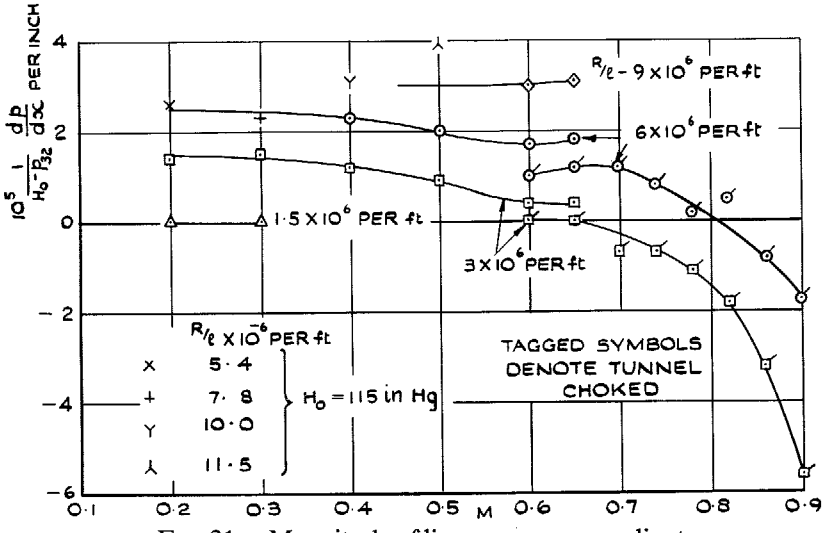

FIG. 21. Magnitude of linear pressure gradient on tunnel centreline.

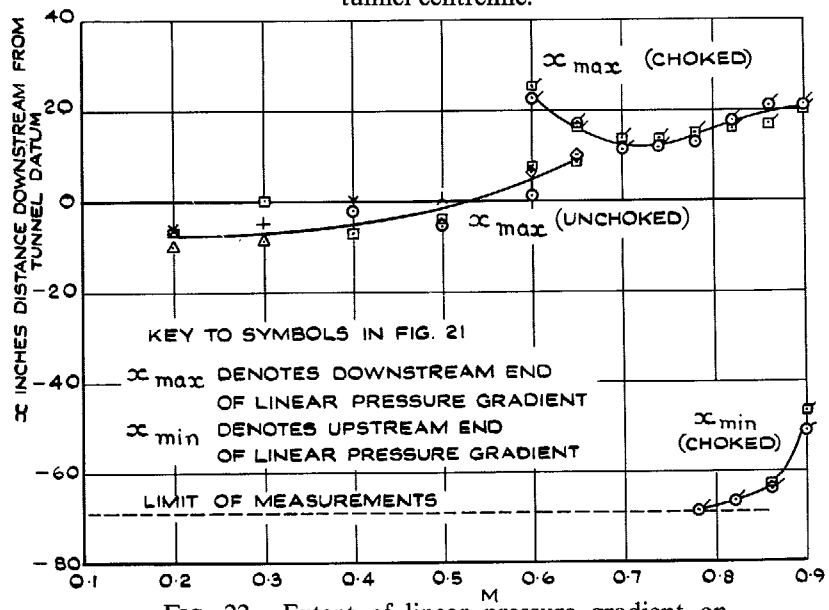

FIG. 22. Extent of linear pressure gradient on tunnel centreline.

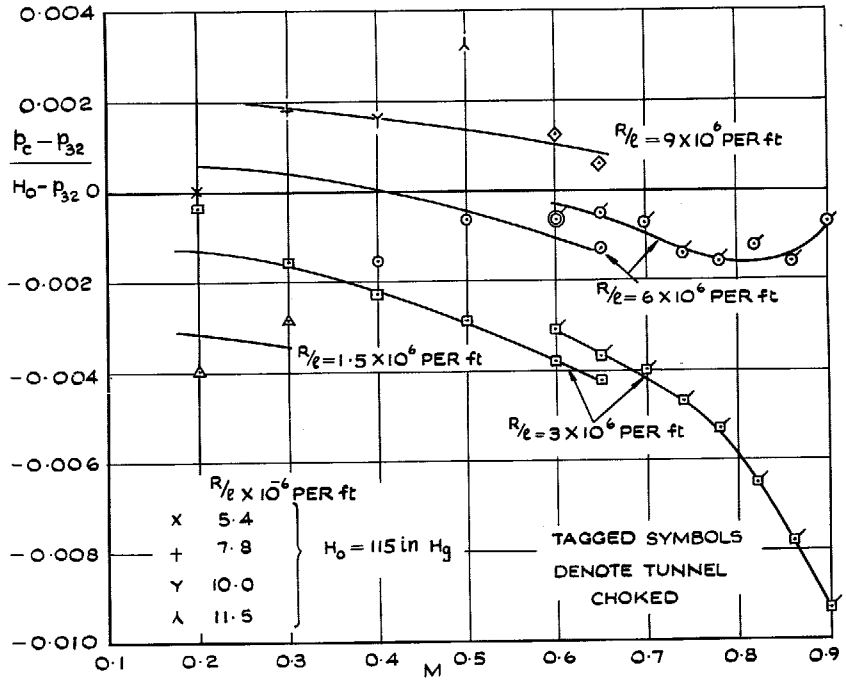

FIG. 23. Intercept of linear pressure gradient with $x = 0$ (tunnel datum).

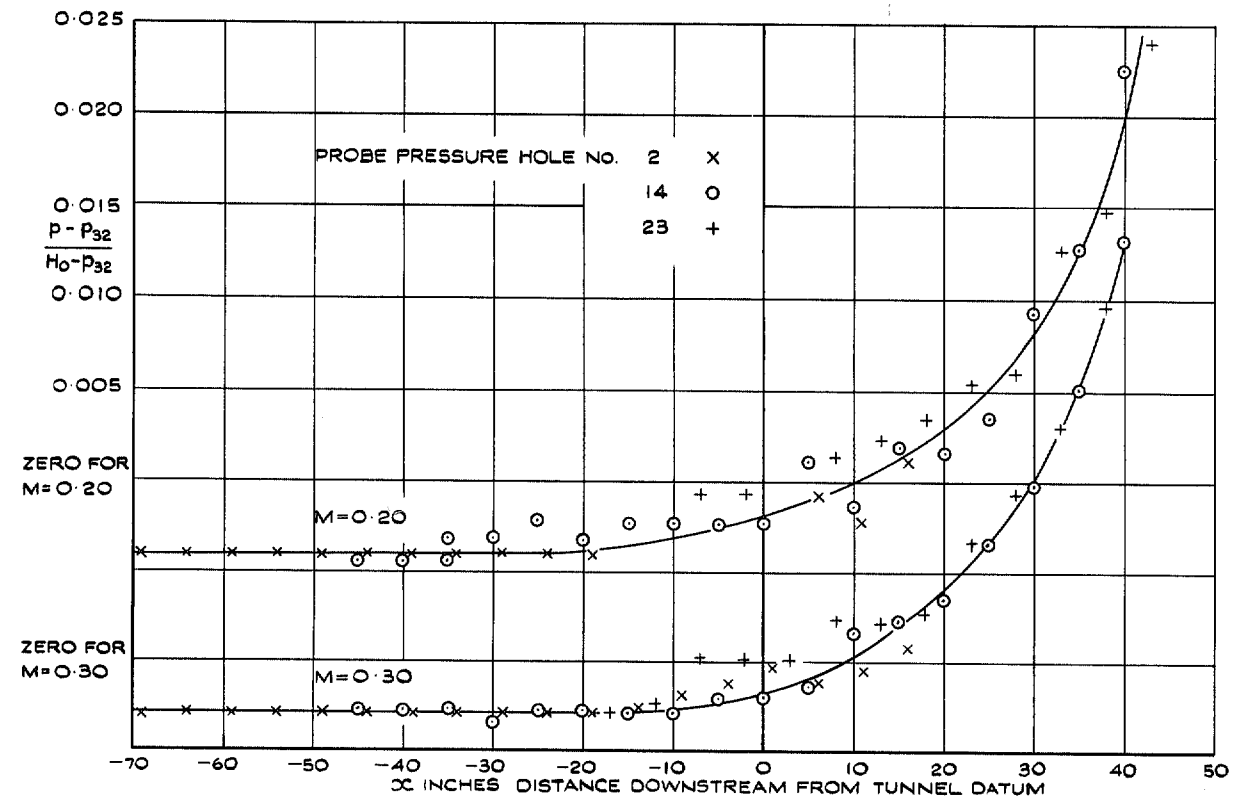

FIG. 24. Tunnel centreline pressure distribution, $M = 0{\cdot}20, 0{\cdot}30$, $R/l = 1{\cdot}5 \times 10^6$ per ft.

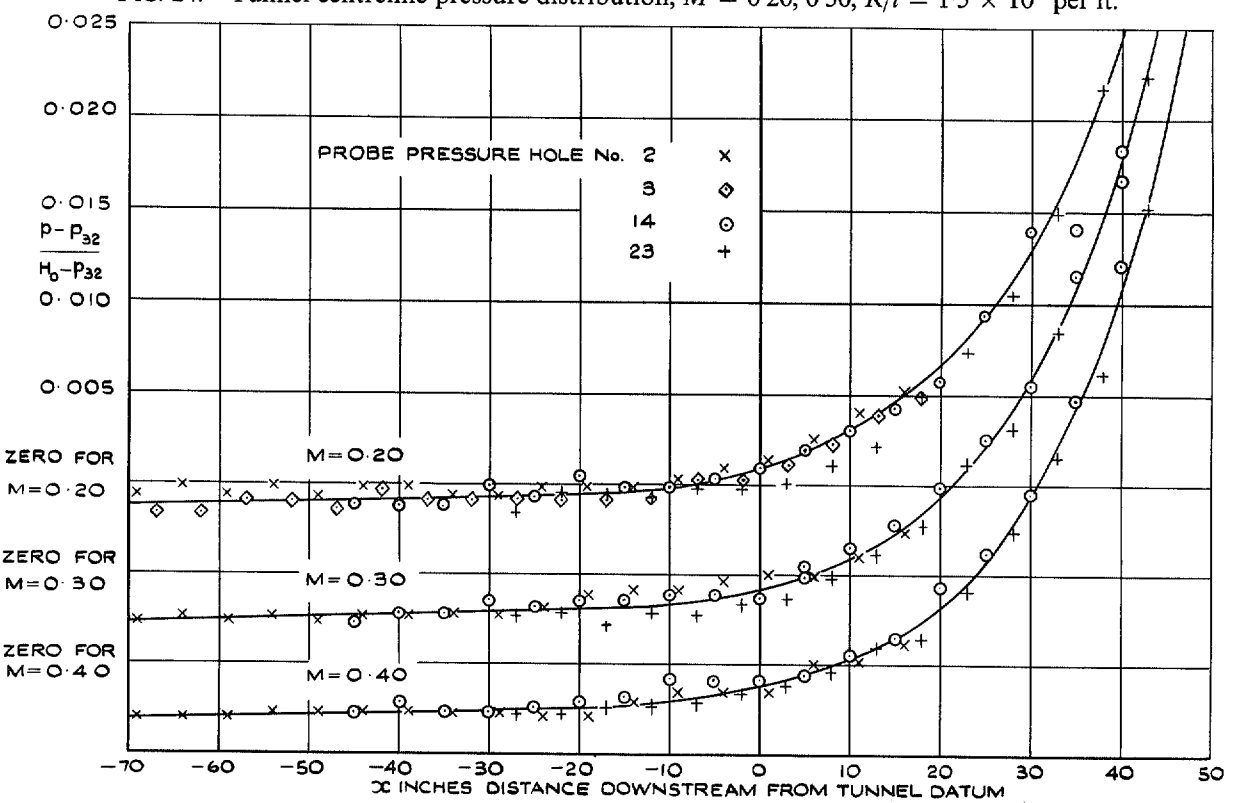

FIG. 25. Tunnel centreline pressure distribution, $M = 0{\cdot}20, 0{\cdot}30, 0{\cdot}40$, $R/l = 3{\cdot}0 \times 10^6$ per ft.

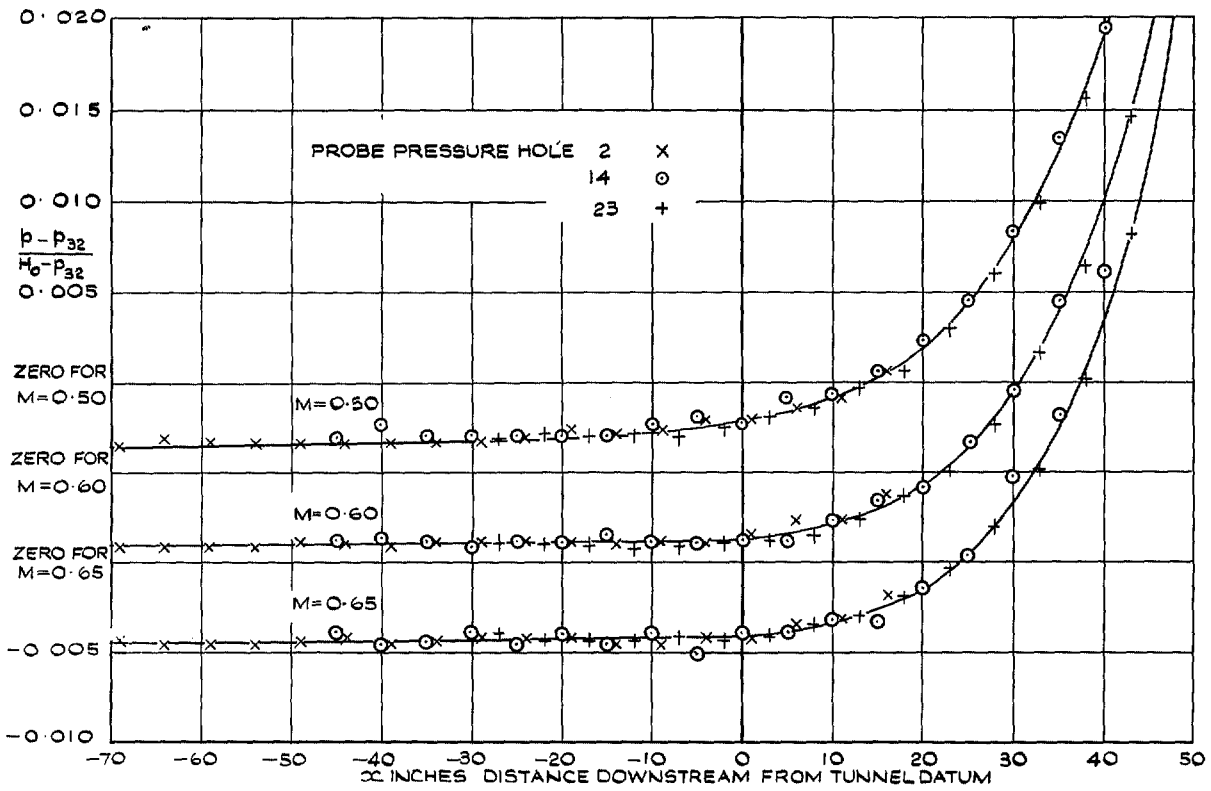

FIG. 26. Tunnel centreline pressure distribution, $M = 0{\cdot}50, 0{\cdot}60, 0{\cdot}65$ (unchoked), $R/l = 3{\cdot}0 \times 10^6$ per ft.

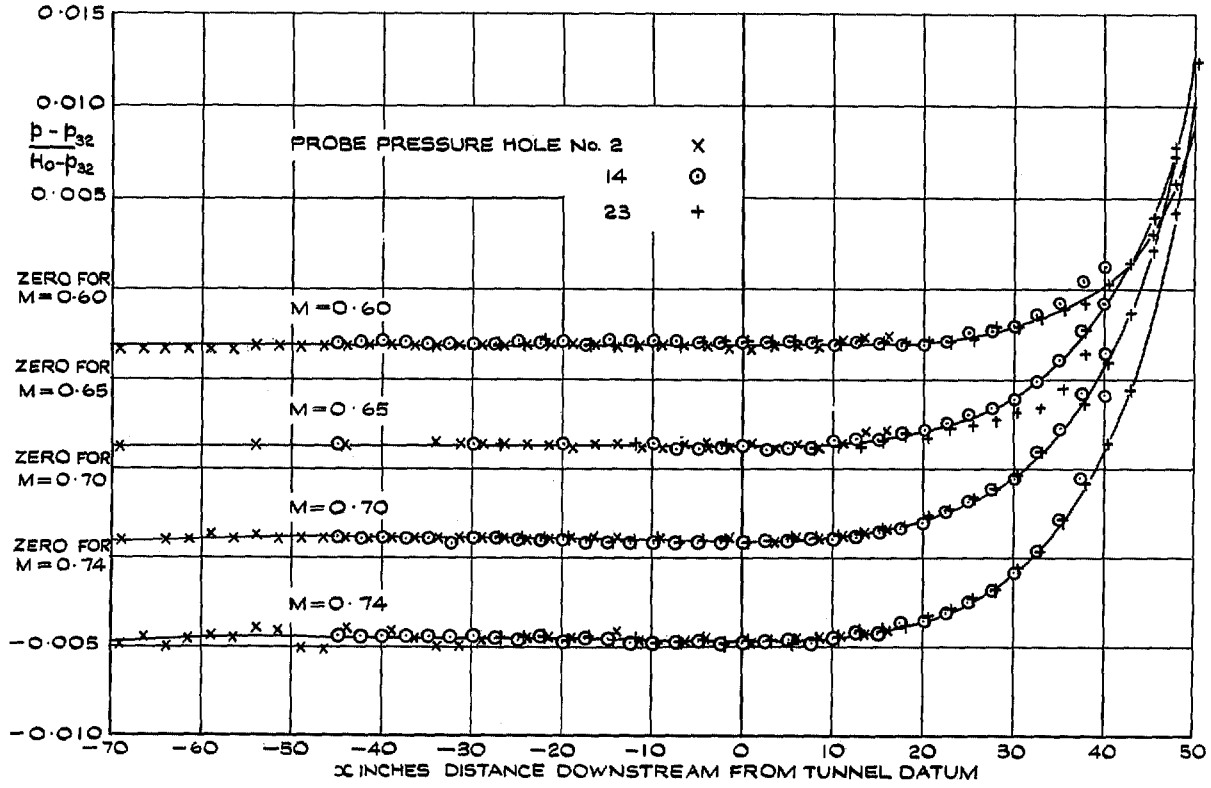

FIG. 27. Tunnel centreline pressure distribution, $M = 0{\cdot}60, 0{\cdot}65, 0{\cdot}70, 0{\cdot}74$ (choked), $R/l = 3{\cdot}0 \times 10^6$ per ft.

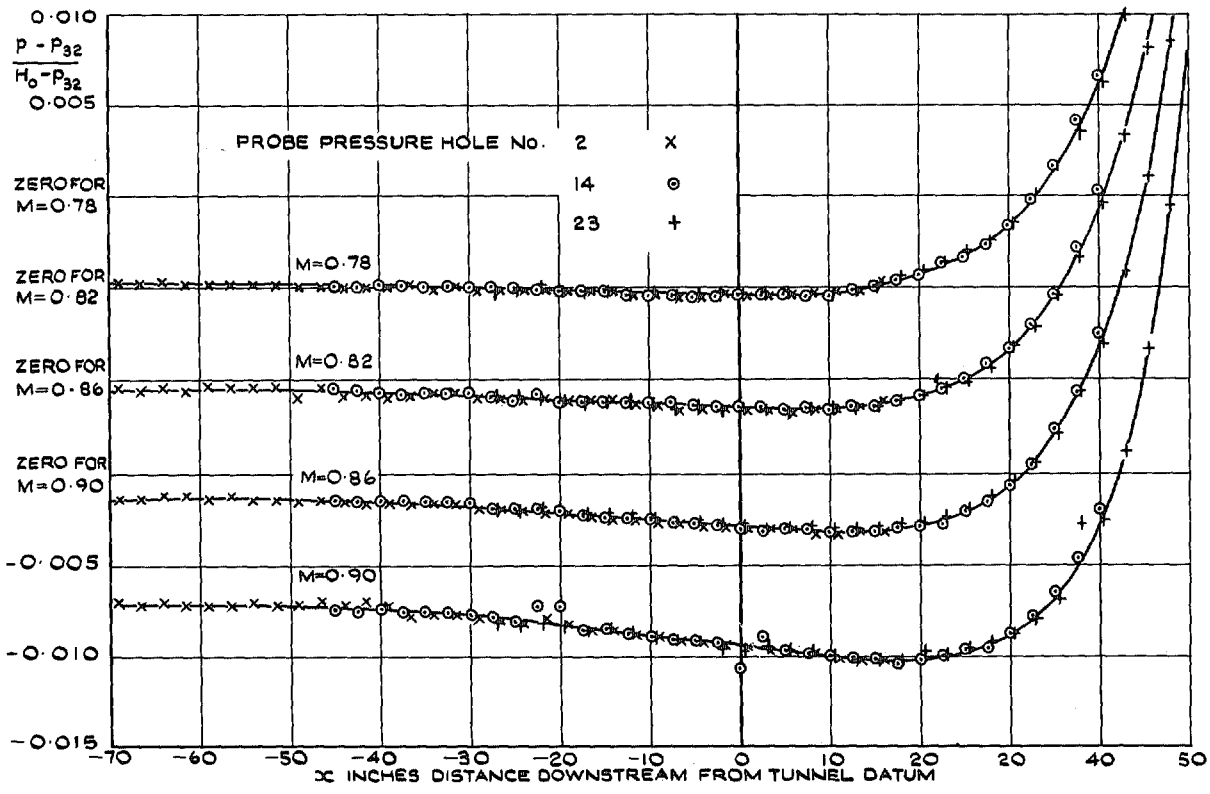

FIG. 28. Tunnel centreline pressure distribution, $M = 0{\cdot}78, 0{\cdot}82, 0{\cdot}86, 0{\cdot}90$, (choked), $R/l = 3{\cdot}0 \times 10^6$ per ft

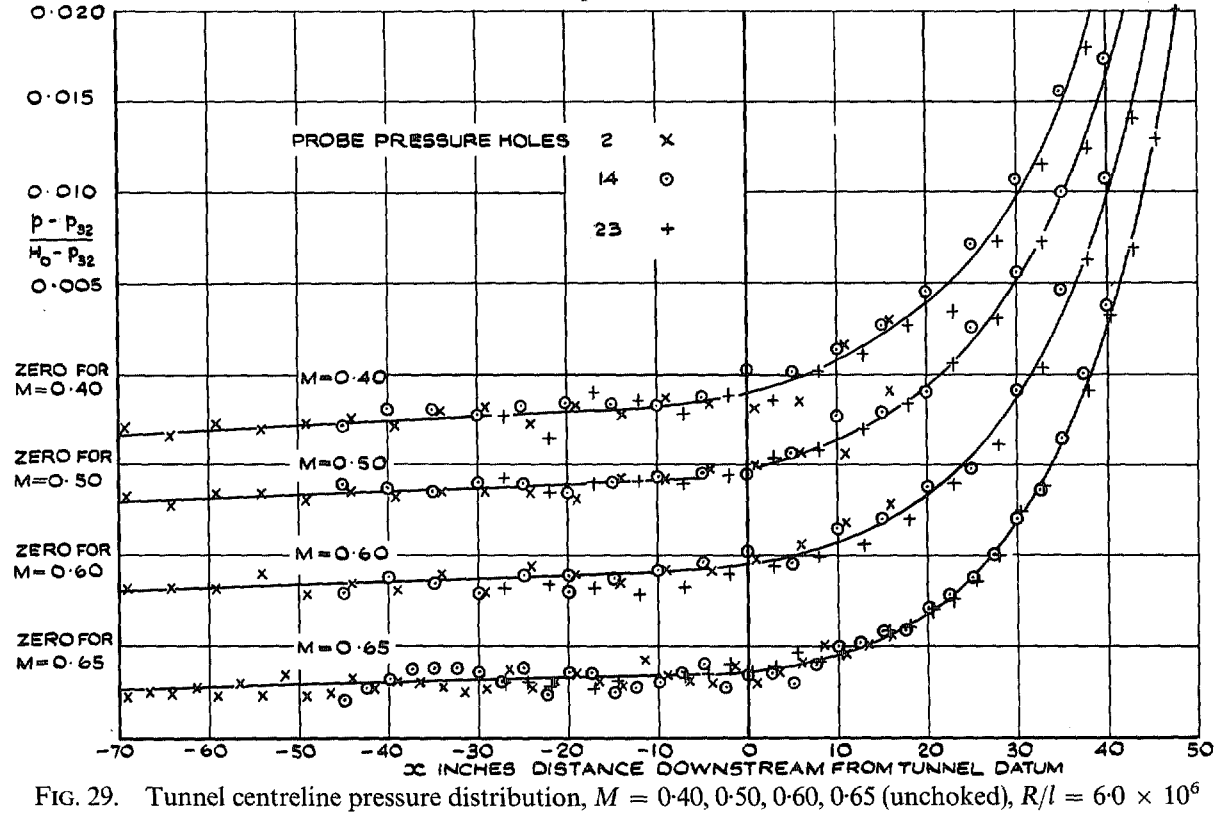

FIG. 29. Tunnel centreline pressure distribution, $M = 0{\cdot}40, 0{\cdot}50, 0{\cdot}60, 0{\cdot}65$ (unchoked), $R/l = 6{\cdot}0 \times 10^6$ per ft.

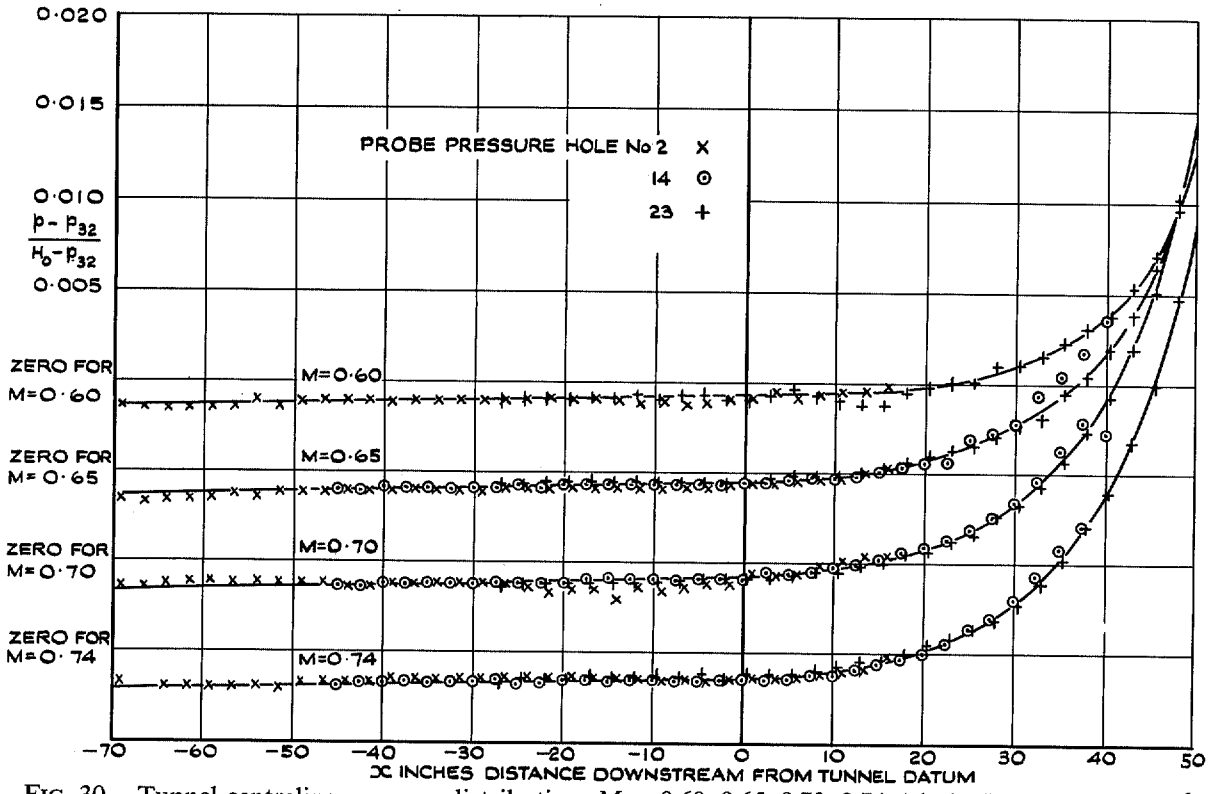

FIG. 30. Tunnel centreline pressure distribution, $M = 0{\cdot}60, 0{\cdot}65, 0{\cdot}70, 0{\cdot}74$ (choked), $R/l = 6{\cdot}0 \times 10^6$ per ft.

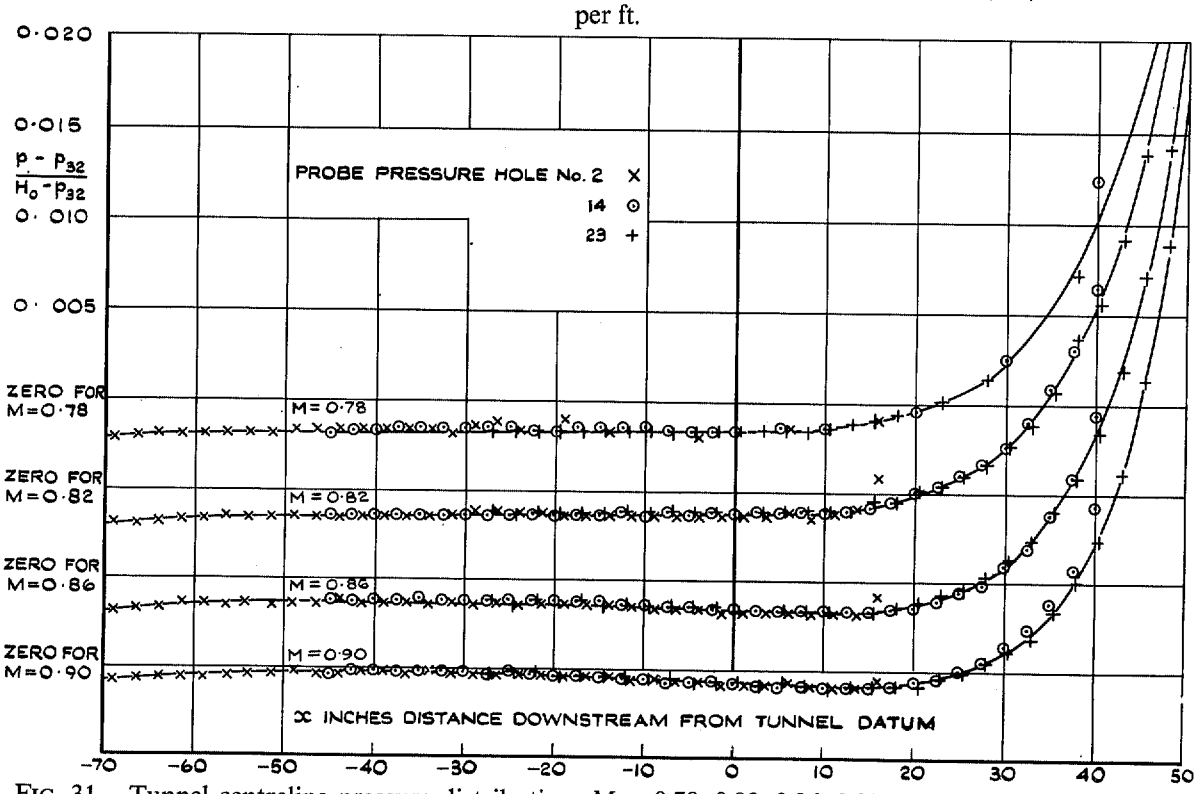

FIG. 31. Tunnel centreline pressure distribution, $M = 0{\cdot}78, 0{\cdot}82, 0{\cdot}86, 0{\cdot}90$ (choked), $R/l = 6{\cdot}0 \times 10^6$ per ft.

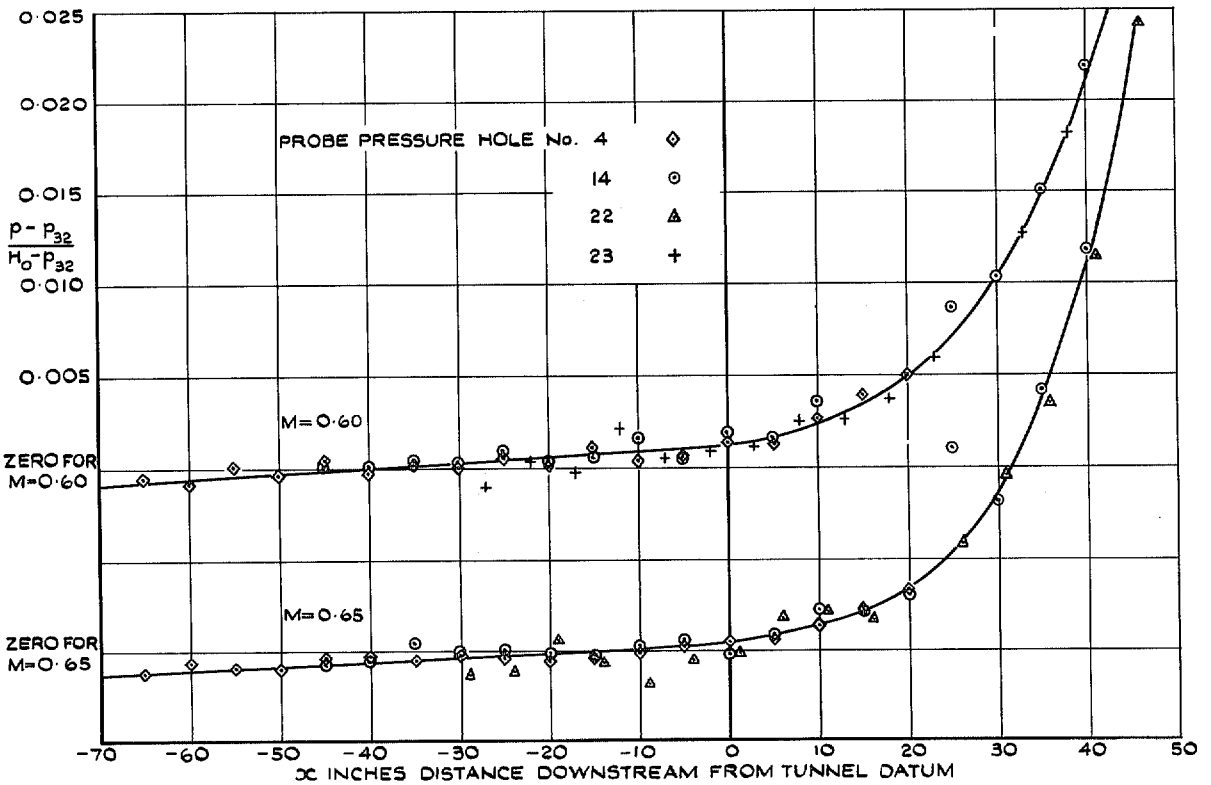

FIG. 32. Tunnel centreline pressure distribution, $M = 0{\cdot}60, 0{\cdot}65$ (unchoked), $R/l = 9{\cdot}0 \times 10^6$ per ft.

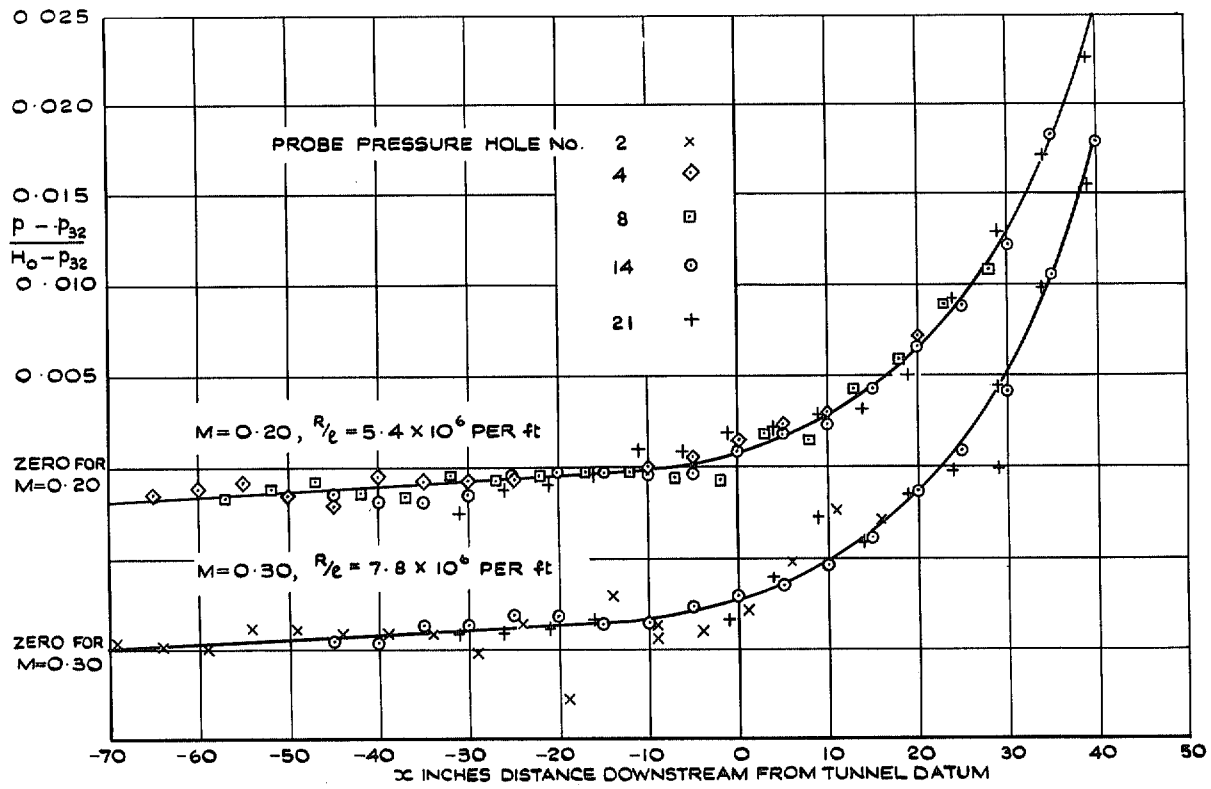

FIG. 33. Tunnel centreline pressure distribution, $M = 0{\cdot}20, 0{\cdot}30$, $H_0 = 115$ inches of mercury.

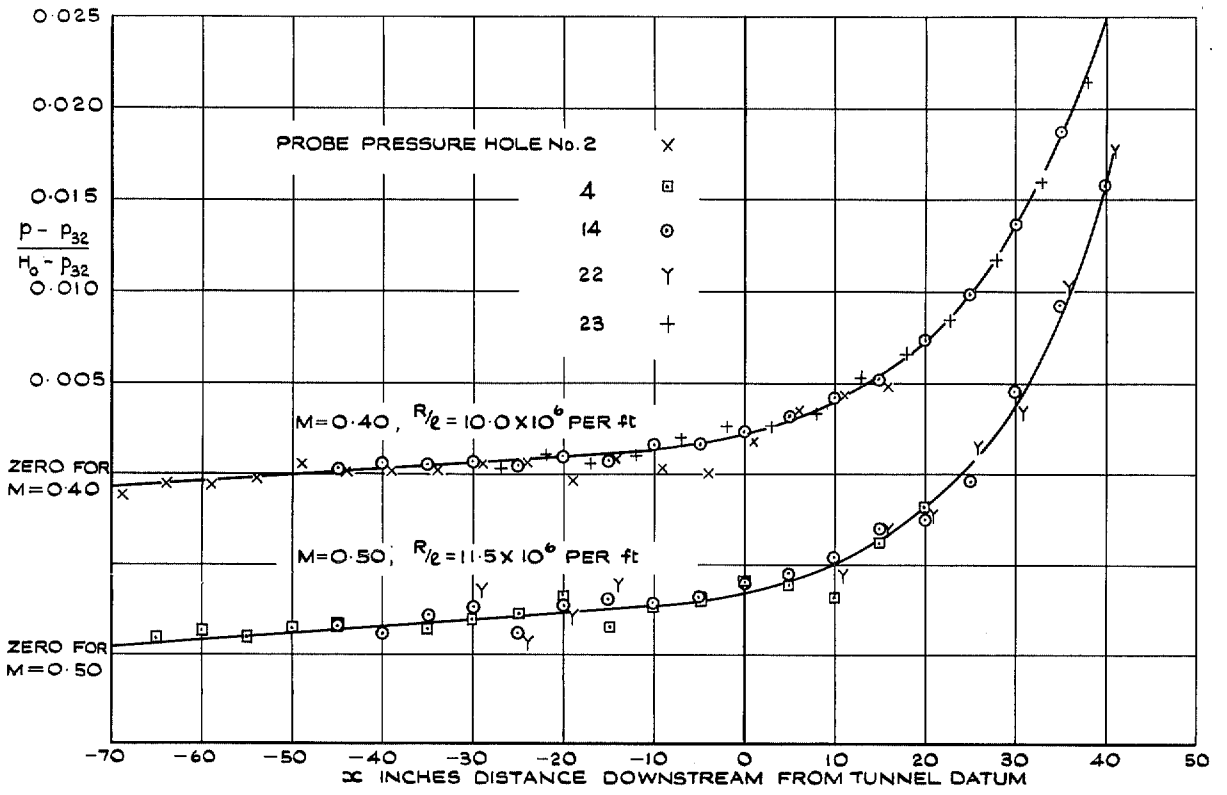

FIG. 34. Tunnel centreline pressure distribution, $M = 0{\cdot}40, 0{\cdot}50, H_0 = 115$ inches of mercury.

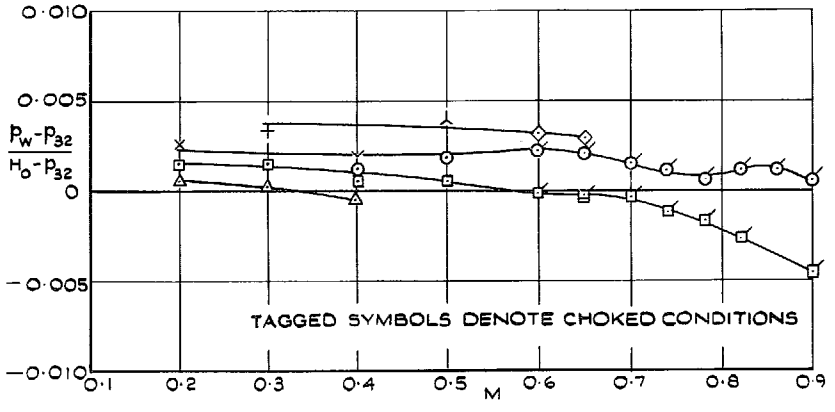

(a) 56 TOP

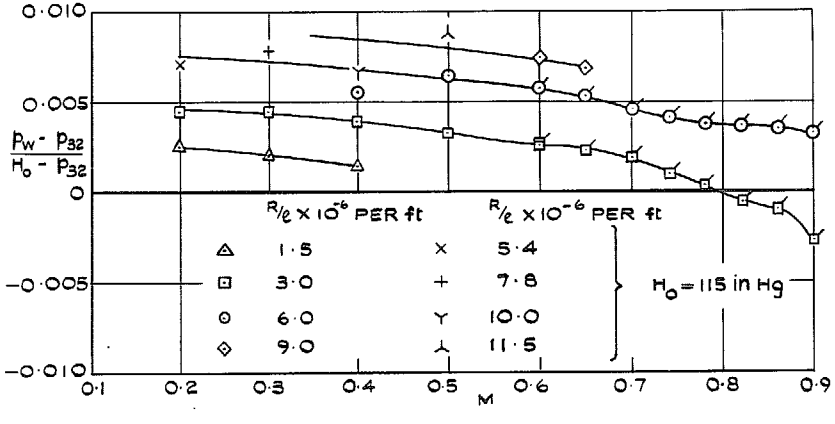

(b) 56 BOTTOM

FIG. 35a & b. Pressure difference between tunnel-wall pressure holes 56 top and 56 bottom and datum static.

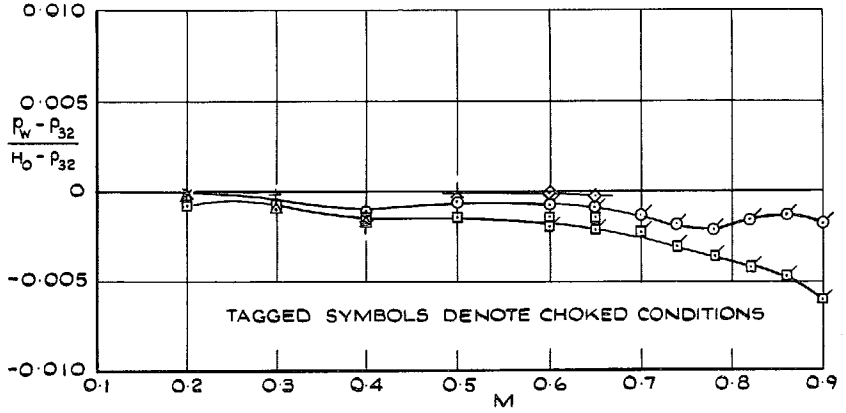

(a) 57 TOP

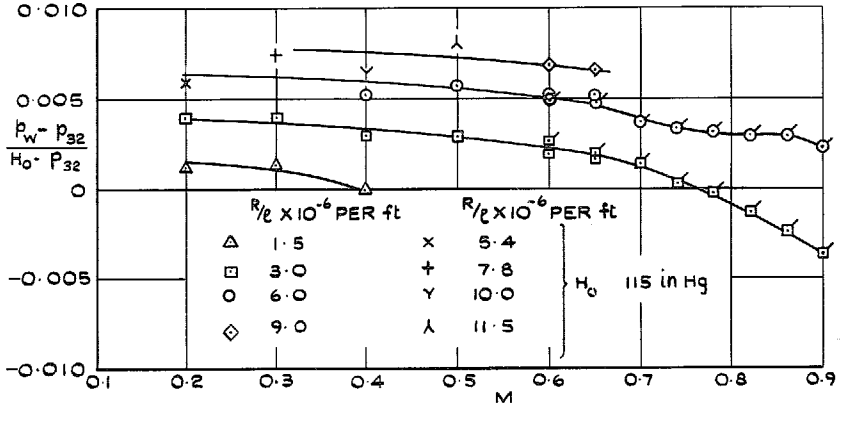

(b) 57 BOTTOM

FIG. 36a & b. Pressure difference between tunnel-wall pressure holes 57 top and bottom and datum static.

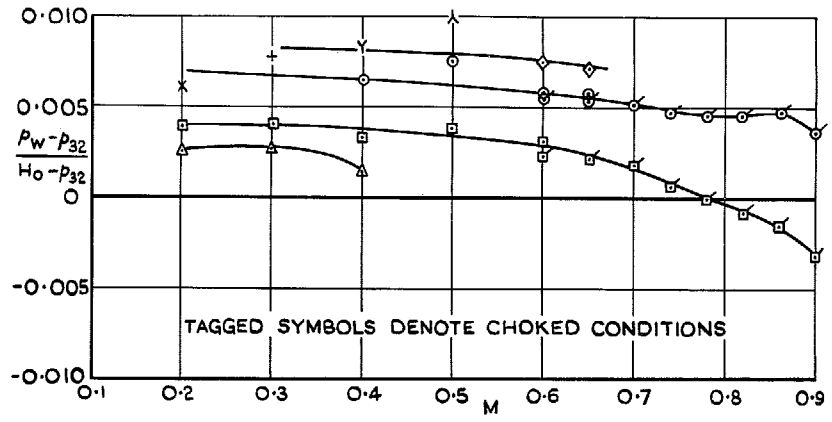

(a) 58 TOP

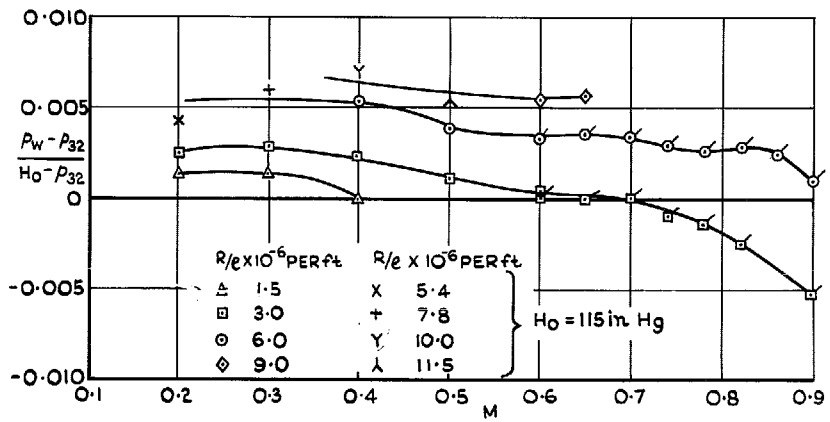

(b) 58 BOTTOM

FIG. 37a & b. Pressure difference between tunnel-wall pressure holes 58 top and bottom and datum static.

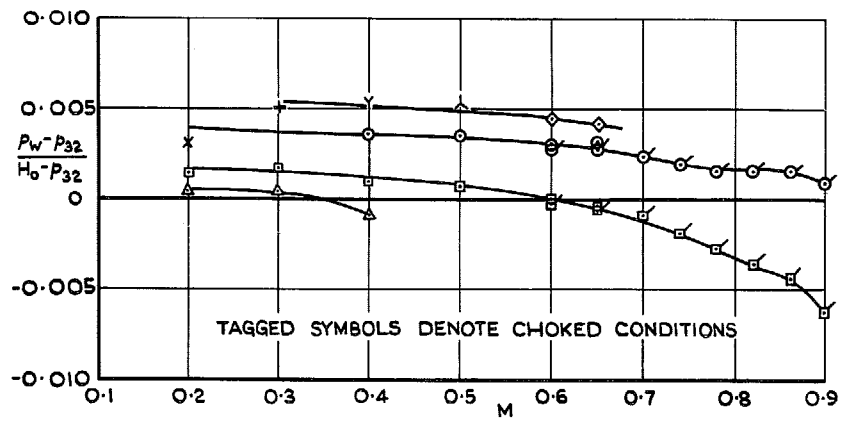

(a) 59 TOP

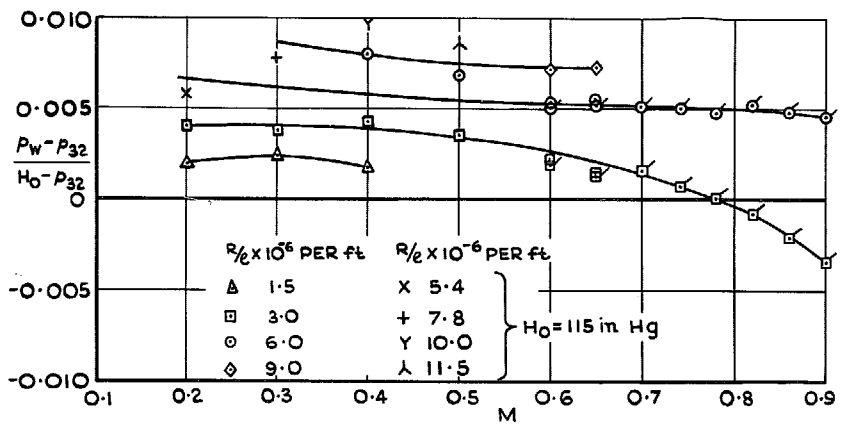

(b) 59 BOTTOM

FIG. 38a & b. Pressure difference between tunnel-wall pressure holes 59 top and bottom and datum static.

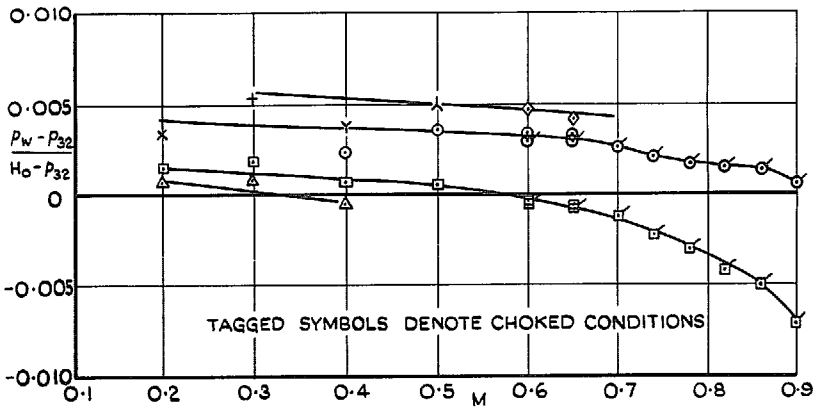

(a) 63 TOP

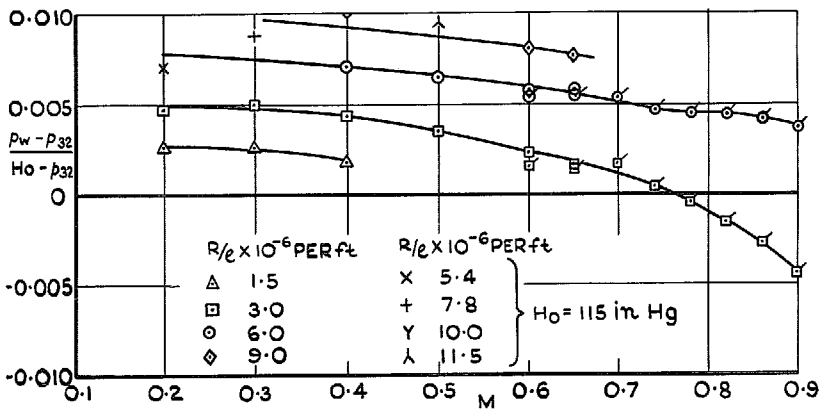

(b) 63 BOTTOM

FIG. 39a & b. Pressure difference between tunnel-wall pressure holes 63 top and bottom and datum static.

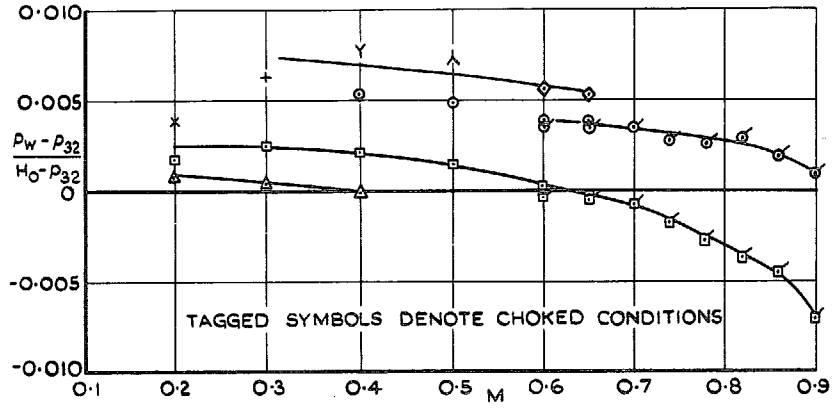

(a) 67 TOP

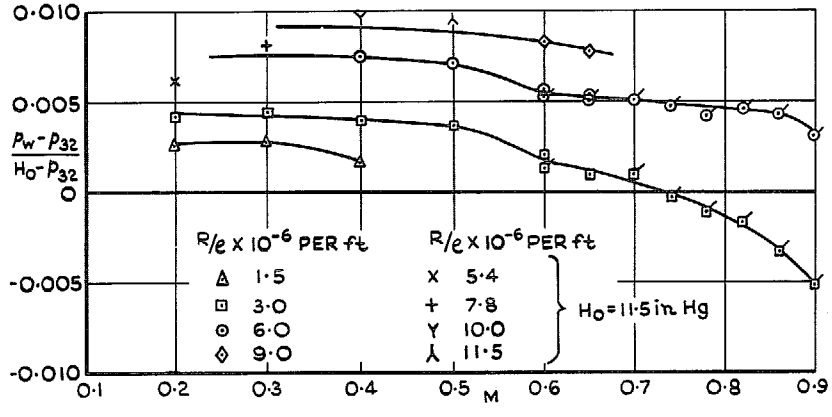

(b) 67 BOTTOM

FIG. 40a & b. Pressure difference between tunnel-wall pressure holes 67 top and bottom and datum static.

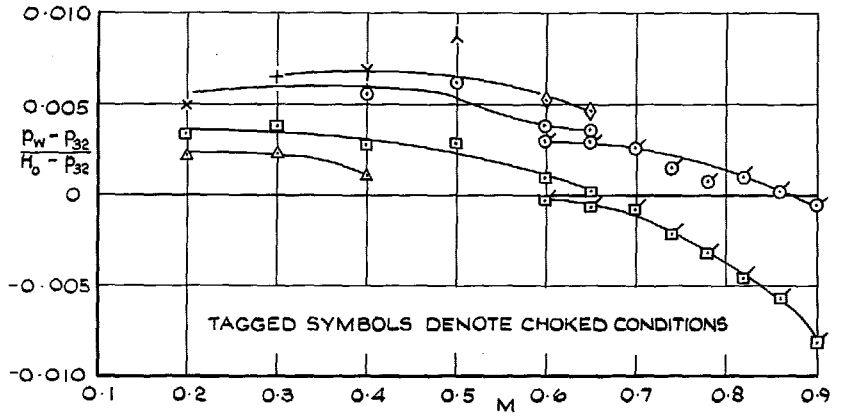

(a) 68 TOP

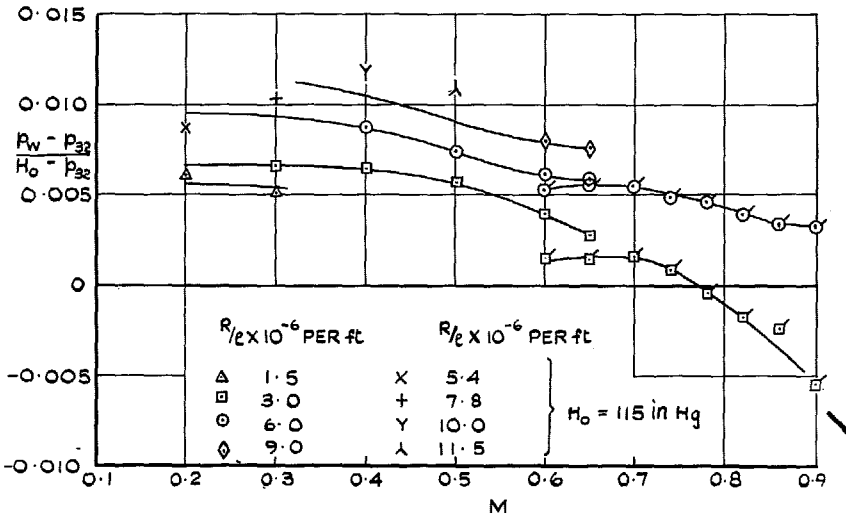

(b) 68 BOTTOM

FIG. 41a & b. Pressure difference between tunnel-wall pressure holes 68 top and bottom and datum static.

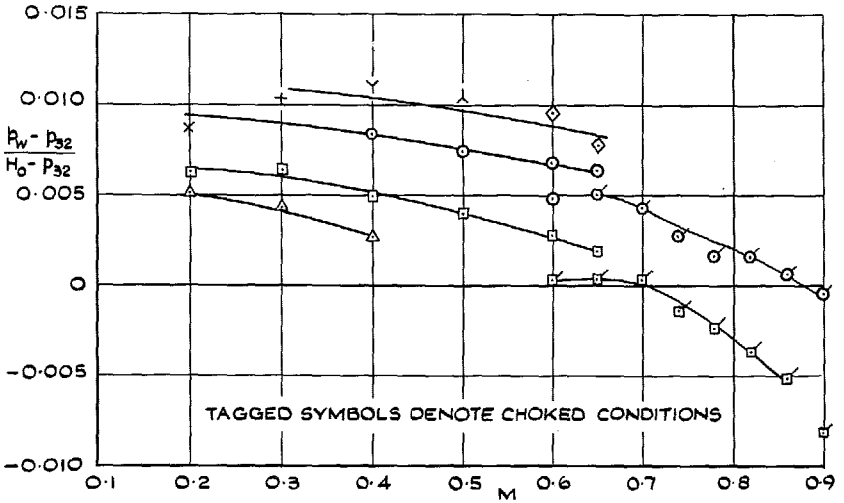

(a) 69 TOP

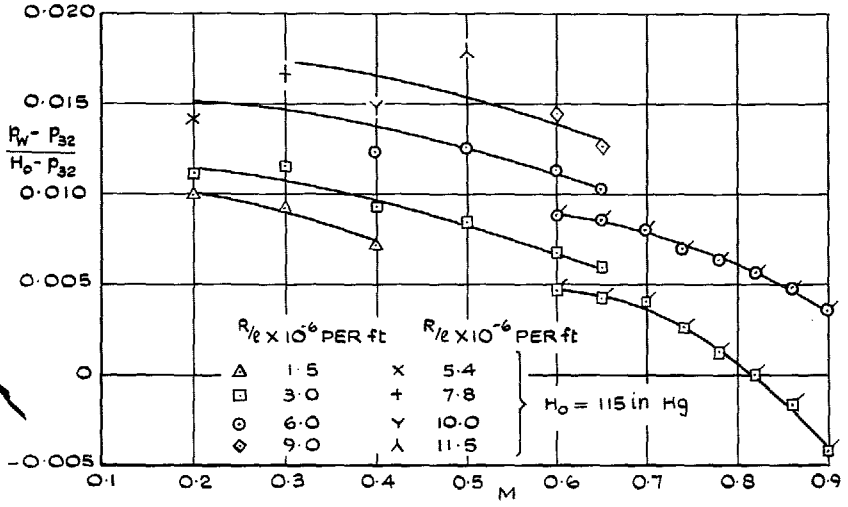

(b) 69 BOTTOM

FIG. 42a & b. Pressure difference between tunnel-wall pressure holes 69 top and bottom and datum static.

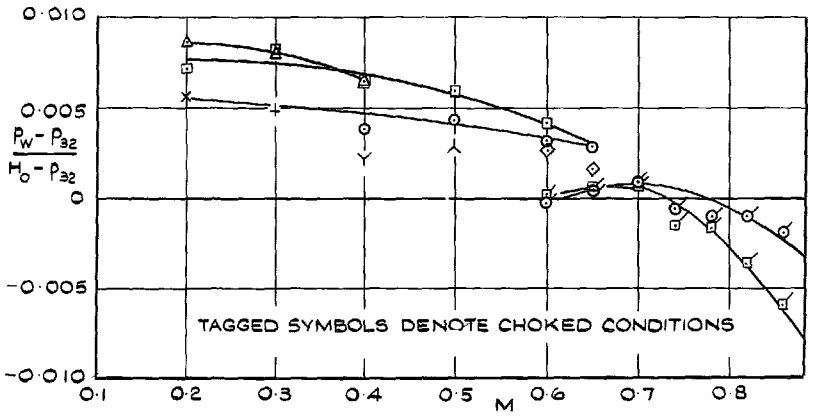

(a) 70 TOP

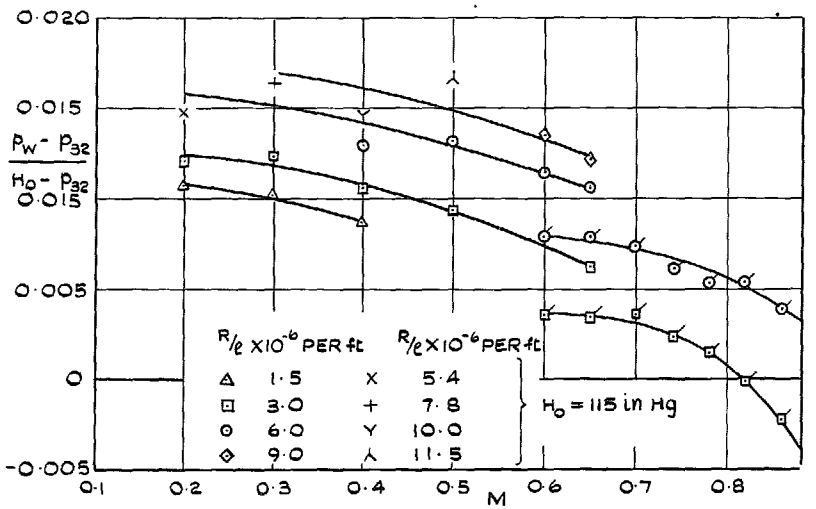

(b) 70 BOTTOM

FIG. 43a & b. Pressure difference between tunnel-wall pressure holes 70 top and bottom and datum static.

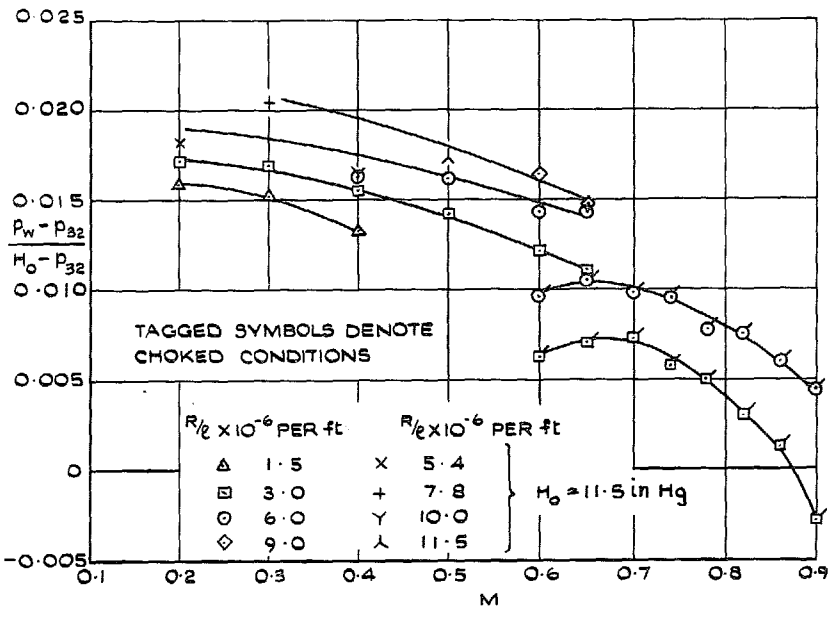

(a) 71 TOP

FIG. 44a. Pressure difference between tunnel-wall pressure holes 71 top and bottom and datum static.

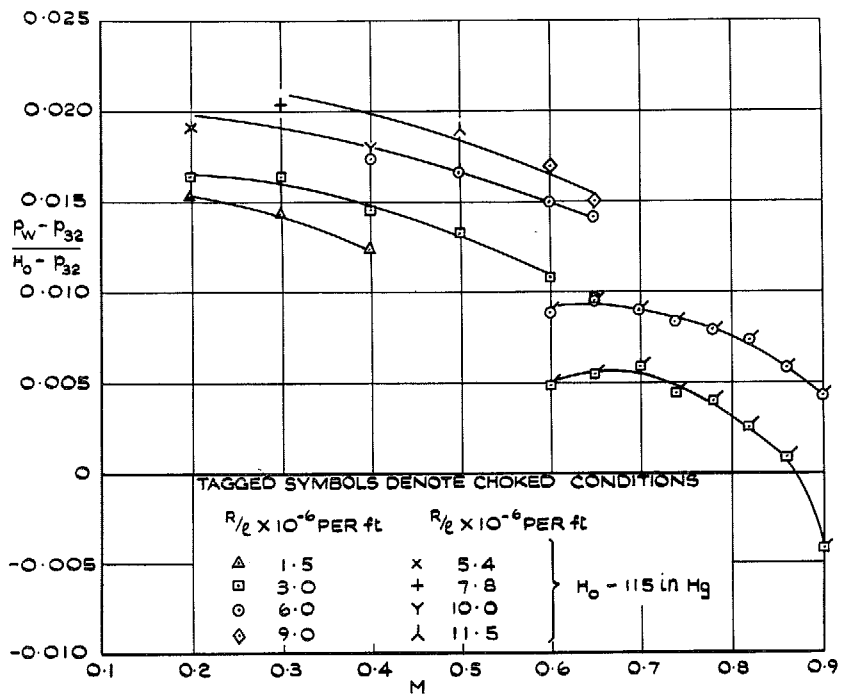

(b) 71 BOTTOM

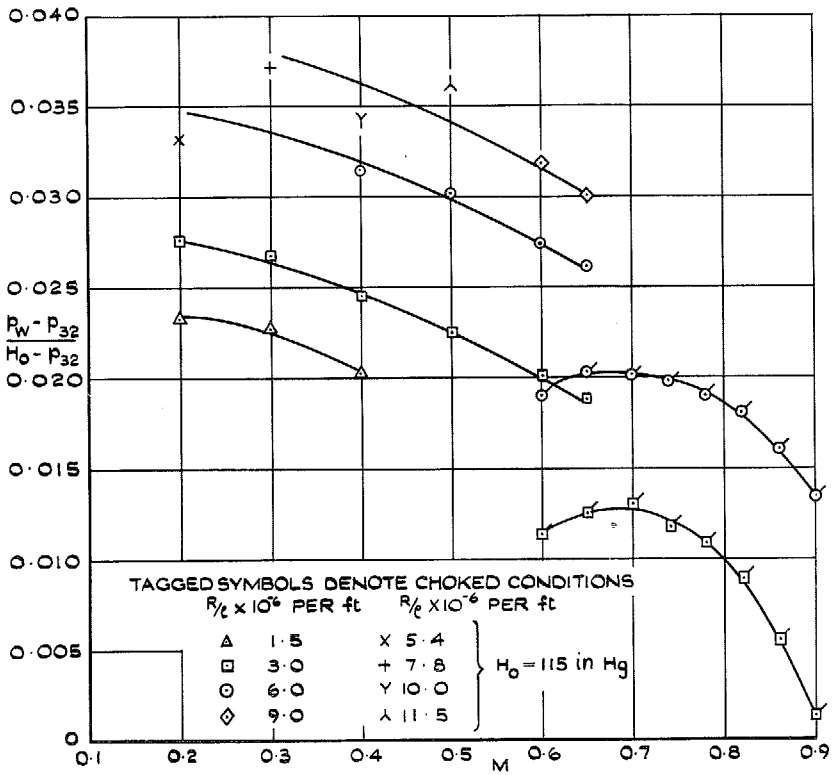

(a) 72 TOP

FIG. 44b. Pressure difference between tunnel-wall pressure holes 71 top and bottom and datum static.

FIG. 45a. Pressure difference between tunnel-wall pressure holes 72 top and bottom and datum static.

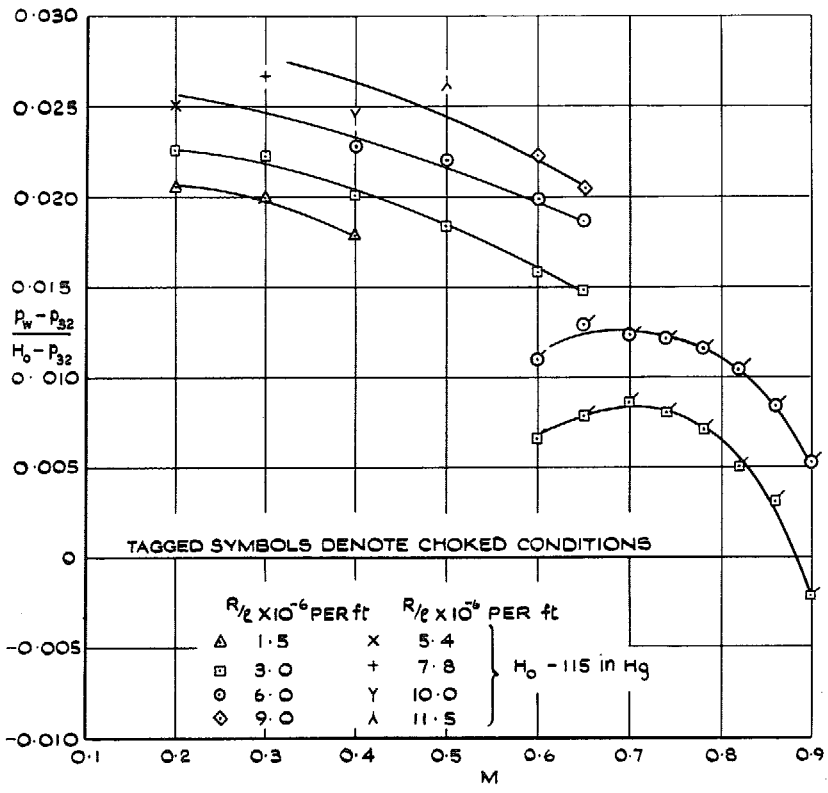

(b) 72 BOTTOM

FIG. 45b. Pressure difference between tunnel-wall pressure holes 72 top and bottom and datum static.

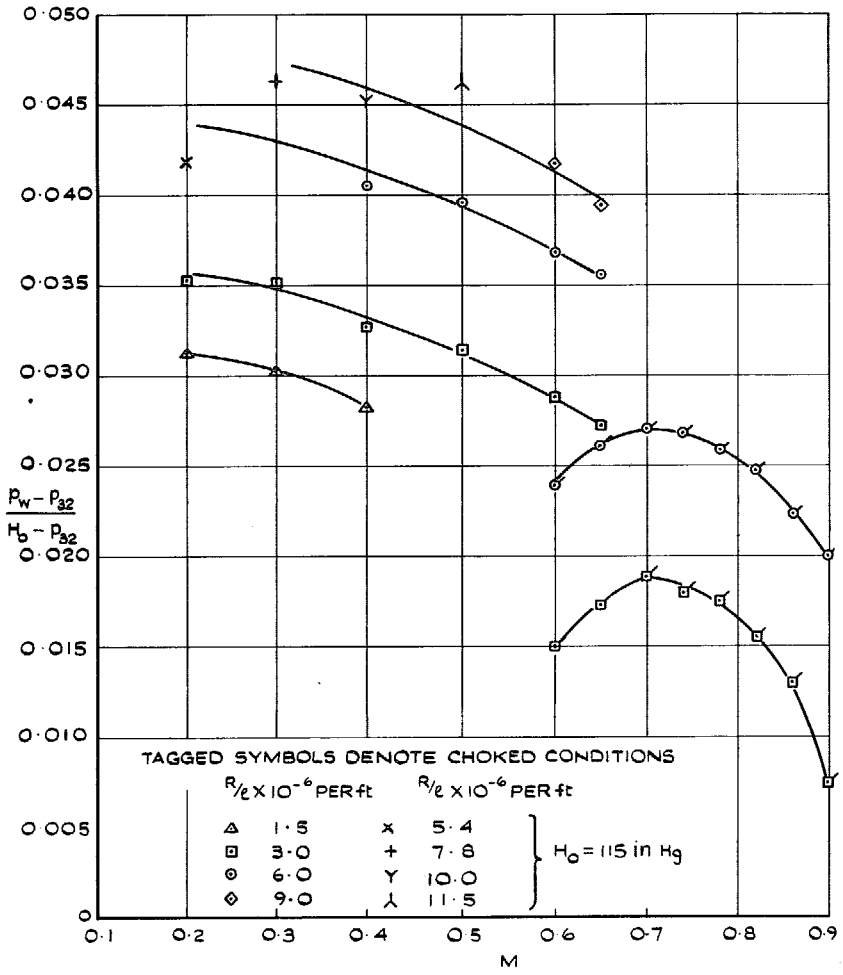

FIG. 46. Pressure difference between tunnel-wall pressure hole 73 top and datum static.

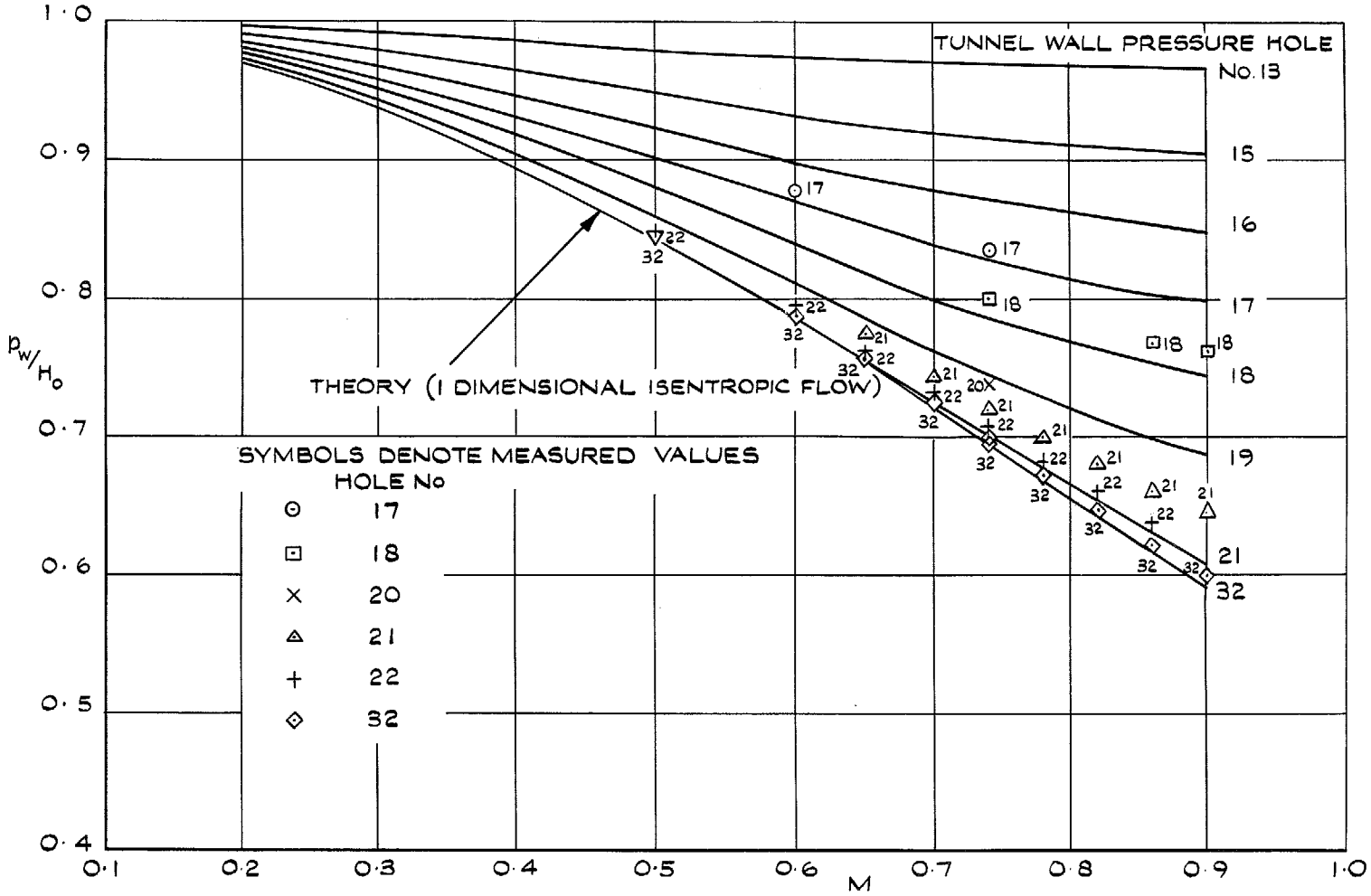

FIG. 47. Variation of static pressure with Mach No. for various tunnel side-wall pressure holes.

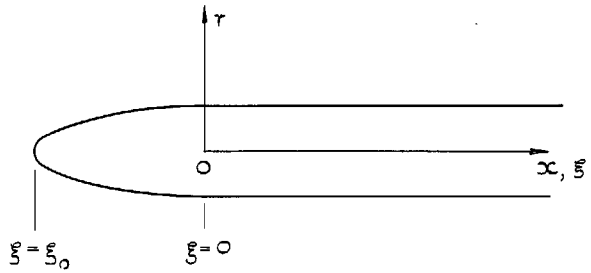

(a) PROBE NOSE

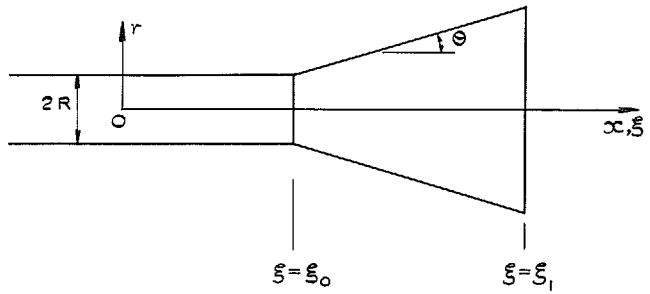

(b) PROBE STING FLARE

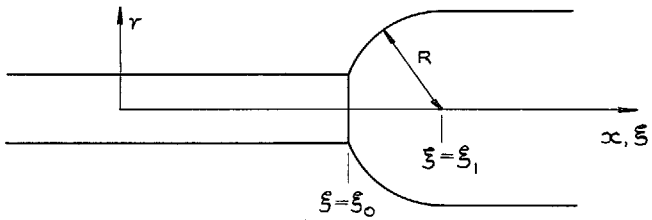

(c) STING FAIRING CAP

FIG. 48a to c. Details of axes used in the calculation of the direct pressure fields of the various probe components.

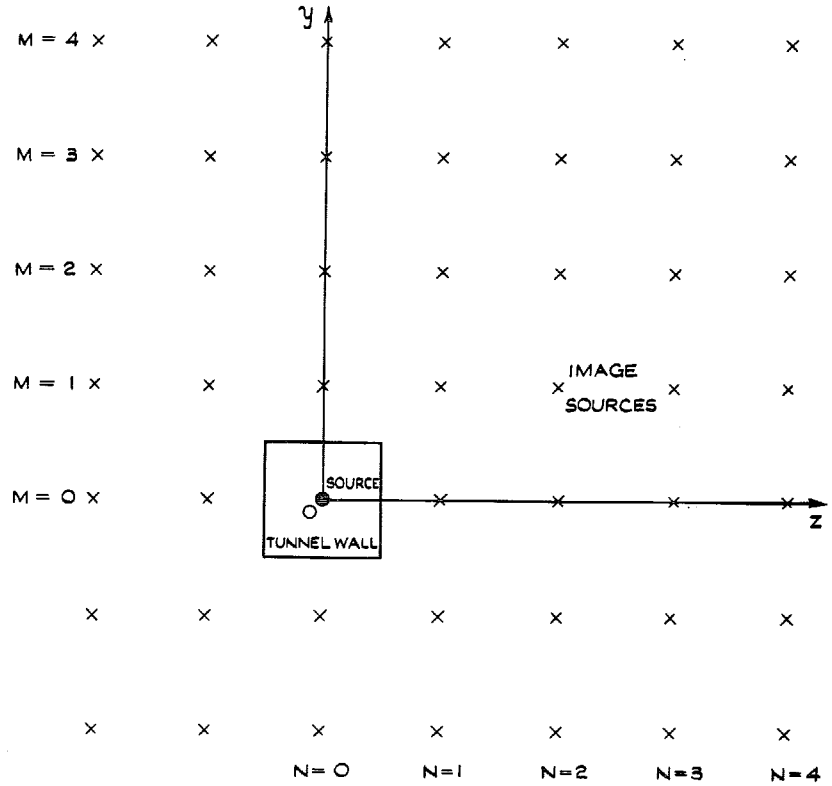

THE x AXIS IS ALIGNED ALONG THE TUNNEL CENTRE LINE WITH x INCREASING DOWNSTREAM

FIG. 49. Arrangement of image sources used to calculate blockage due to a single source on tunnel centreline.

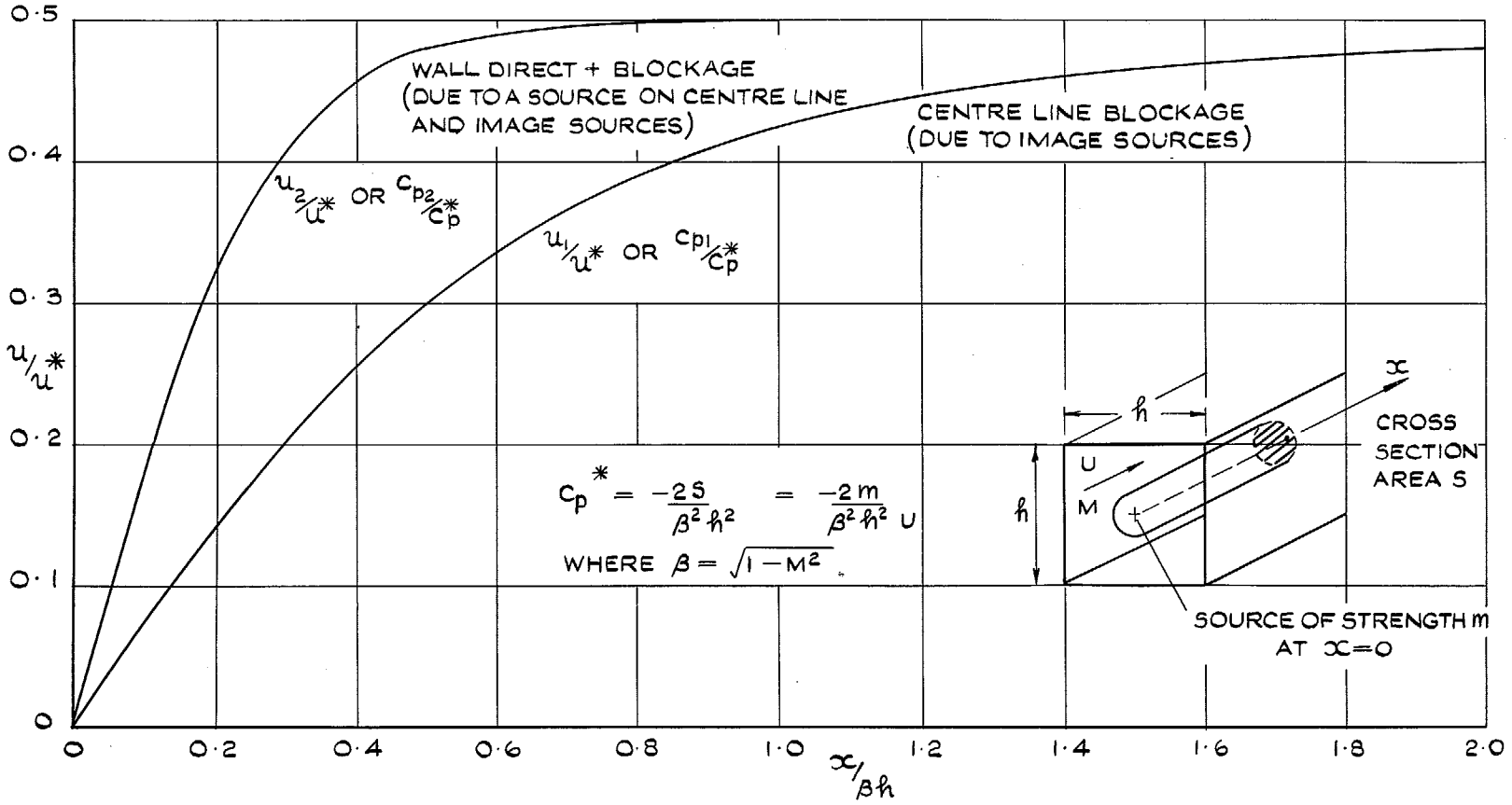

FIG. 50. Static pressure distribution along centreline and centre of wall of a square tunnel due to a source on the centreline.

Printed in Wales for Her Majesty's Stationery Office by Allens Printers (Wales) Ltd.

Dd. 135646 K.5.

Published by
HER MAJESTY'S STATIONERY OFFICE

To be purchased from
49 High Holborn, London W.C.1
13A Castle Street. Edinburgh EH2 3AR
109 St. Mary Street, Cardiff CF1 1JW
Brazennose Street, Manchester M60 8AS
50 Fairfax Street, Bristol BS1 3DE
258 Broad Street, Birmingham 1
7 Linenhall Street, Belfast BT2 8AY
or through any bookseller

R. & M. No. 3583

SBN 11 470199 7